Breast Cancer Research

RESEARCH

Open Access

Unveiling the key mechanisms of FOLR2+ macrophage-mediated antitumor immunity in breast cancer using integrated single-cell RNA sequencing and bulk RNA sequencing

Sixuan Wu[1,2†], Baohong Jiang[3†], Zhimin Li[1†], Yuanbin Tang[1], Lunqi Luo[1], Wenjie Feng[1], Yiling Jiang[1], Yeru Tan[1*] and Yuehua Li[1*]

Abstract

Breast cancer (BRCA) is a common malignant tumor, and its immune microenvironment plays a crucial role in disease progression. In this research, we utilized single-cell RNA sequencing and bulk RNA sequencing technologies, combined with in vivo and in vitro experiments, to thoroughly investigate the immunological functions and mechanisms of FOLR2+ macrophages in BRCA. Our findings demonstrate a significant enhancement in the interaction between FOLR2+ macrophages and $CD8^+$ T cells within the tumor tissues of BRCA patients. FOLR2 is closely associated with T cell infiltration in the tumor microenvironment of BRCA patients, particularly with $CD8^+$ T cells. By secreting CXCL9 and engaging with CXCR3, FOLR2+ macrophages can activate the functionality of $CD8^+$ T cells, thereby promoting cancer cell apoptosis. Further animal experiments confirm that FOLR2+ macrophages activate $CD8^+$ T cells through the CXCL9-CXCR3 axis, exhibiting an antitumor immunity effect in BRCA. FOLR2+ macrophages play a crucial role in antitumor immunity in BRCA through the CXCL9-CXCR3 axis.

Keywords BRCA, FOLR2+ macrophages, $CD8^+$ T cells, CXCL9-CXCR3 axis, Single-cell RNA sequencing, Immune microenvironment

Introduction

Breast cancer (BRCA) is one of the most prevalent malignant tumors among women worldwide, with increasing incidence and mortality rates annually [1–3]. The development and progression of BRCA are associated with various factors, among which the immune microenvironment plays a crucial role [4–7]. In recent years, researchers have increasingly recognized the pivotal role of tumor-associated macrophages (TAMs) in tumor initiation, progression, and immune evasion [8–11]. As a member of immune cells, macrophages can be classified into M1 (pro-inflammatory) and M2 (anti-inflammatory) subtypes based on their functions and phenotypic characteristics, with M2 macrophages closely associated with tumor growth, metastasis, and immune suppression [12].

†Sixuan Wu, Baohong Jiang and Zhimin Li contributed equally as co-first authors.

*Correspondence:
Yeru Tan
tanyeru@163.com
Yuehua Li
liyuehua2020@stu.usc.edu.cn
[1] Department of Oncology, the First Affiliated Hospital, Hengyang Medical School, University of South China, No. 69 Chuanshan Road, Hengyang 421001, Hunan Province, People's Republic of China
[2] Clinical Oncology School of Fujian Medical University, Fujian Cancer Hospital, Fuzhou 350014, Fujian, People's Republic of China
[3] Department of Pharmacy, the First Affiliated Hospital, Hengyang Medical School, University of South China, Hengyang 421001, Hunan Province, People's Republic of China

FOLR2 is a membrane protein associated with folate metabolism, garnering attention from researchers in the context of BRCA in recent years [13, 14]. Some studies have found a significant increase in FOLR2 expression in BRCA, closely related to the pathogenesis and prognosis of the disease [15]. Research in ovarian cancer, colorectal cancer, and other solid tumors has indicated a connection between FOLR2+ macrophages and immune suppression, enhanced cell proliferation, and invasiveness of tumors [13, 16, 17]. Moreover, $CD8^+$ T cells, as crucial cytotoxic immune cells, are believed to play a key role in tumor immunotherapy within the tumor microenvironment (TME) [18–20]. However, the relationship between FOLR2+ macrophages and $CD8^+$ T cells and their roles in BRCA remains unclear [21].

Single-cell RNA sequencing (scRNA-seq) technology has provided a novel tool and perspective for investigating cell heterogeneity within the TME [22]. In comparison to traditional bulk RNA sequencing (bulk RNA-seq) techniques, scRNA-seq can reveal gene expression differences at the level of individual cells, offering a more precise description of functional states and interactions among cells [23]. This technology allows for in-depth exploration of various cell types within the TME, such as tumor cells, immune cells, and stromal cells, to investigate their interactions and communication [24].

Given the aforementioned background and technological advancements, this study aims to delve into the functions of FOLR2+ macrophages in BRCA and their relationship with $CD8^+$ T cells through the integration of scRNA-seq and bulk RNA-seq techniques, coupled with in vitro and in vivo experiments. By elucidating how FOLR2+ macrophages impact $CD8^+$ T cell activation through the CXCL9-CXCR3 pathway and contribute to antitumor immunity in BRCA, it is hoped that this research will offer new strategies and targets for the treatment of BRCA.

Materials and methods

Data retrieval from public databases

The TCGA-BRCA (BRCA) dataset was retrieved from The Cancer Genome Atlas (TCGA) database (https://portal.gdc.cancer.gov/), and RNA expression data (HTSeq-FPKM) and clinical information for 1113 tumor tissue samples and 113 adjacent normal tissue samples from BRCA patients were downloaded in June 2023. The METABRIC dataset was obtained through the cBioPortal database (http://www.cbioportal.org/), comprising RNA expression data (HTSeq-FPKM) and clinical information of 1017 BRCA patient tumor tissue samples. Furthermore, the BRCA dataset was sourced from the Clinical Proteomic Tumor Analysis Consortium (CPTAC) database (https://proteomics.cancer.gov/), involving the download of protein expression data and clinical information of 18 healthy control breast tissue samples and 125 BRCA patient tumor tissue samples [25]. Since these data originate from a public database, ethical committee approval is not required.

Clinical sample collection

This study retrospectively collected 25 samples of normal breast tissue and 48 samples of BRCA tumor tissue from our hospital, along with their clinical data (Table S1). The normal breast tissue and BRCA tumor tissue samples were freshly frozen in liquid nitrogen and stored at −80 °C. Prior to utilizing these clinical resources for investigation, all patients provided informed consent, and the experiment was approved by the Ethics Committee of the First Affiliated Hospital, Hengyang Medical School, University of South China (No. 2022-11-126), following the guidelines of the Helsinki Declaration.

scRNA-seq

Four normal breast tissue samples (N1–N4) and four BRCA tumor tissue samples (T1–T4) were collected for scRNA-seq. Tumor samples were obtained from two ER+, one HER2+, and one TNBC case. The normal and tumor samples were strictly matched in terms of donor age and menopausal status.

First, the tissues were processed using trypsin (9002-07-7, Sigma Aldrich, USA) and collagenase I (C0130, Sigma Aldrich, USA) with a dissociation time controlled within four hours to minimize cell loss and transcriptomic alterations, avoiding overnight dissociation that may lead to cellular component changes [26]. DNase I (10104159001, Roche, Switzerland) was added during the dissociation to reduce cell clustering. Single-cell suspensions were obtained by filtering through a 40 μm cell strainer. Cell viability was assessed using trypan blue staining, ensuring viability > 85%.

Single cells were captured using the 10× Genomics Chromium system. Once captured, cells were lysed on the chip, releasing mRNA, which was reverse transcribed to generate cDNA. After lysis and reverse transcription, the cDNA was pre-amplified in a microfluidic chip for subsequent sequencing. The amplified cDNA was used for library construction and sequenced on the HiSeq 4000 Illumina platform (paired-end reads, 2×75 bp, approximately 20,000 reads per cell) [27].

Using the Cellranger software provided by 10× Genomics, an expression matrix was generated. Cells expressing more than 200 genes (nFeature_RNA > 200), with fewer than 50,000 RNA counts (nCount_RNA < 50,000), and with mitochondrial gene content below 15% (percent.mt < 15%) were retained. The filtered data quality was

further assessed through a unique molecular identifier and gene correlation analysis [27].

UMAP clustering analysis and cell annotation

The Harmony method was used in Seurat to correct batch effects and integrate scRNA-seq data from normal and tumor breast tissues. Principal component analysis was performed on the data using the top 2000 highly variable genes based on variance. The selection of principal components for downstream analysis was determined by integrating the JackStrawPlot and ElbowPlot functions. The Seurat-provided FindClusters function was utilized to identify major cell subpopulations, with a resolution set at 0.5. Subsequently, the UMAP algorithm was applied to perform non-linear dimensionality reduction and obtain a two-dimensional visualization of the scRNA-seq sequencing data. Marker genes specific to various cell subpopulations were identified using the findmarkergenes function from the scCATCH package. Cell types were manually annotated based on known cell marker genes [28].

Malignant cell extraction

After extracting epithelial cells using the subset function, copy number variation (CNV) analysis was performed using the inferCNV package. The K-means algorithm was then applied to eliminate non-malignant cells within the epithelial population. Subsequently, malignant cells were subjected to UMAP clustering analysis [29, 30].

Analysis of cellular communication

CellCall is a toolkit designed to infer intercellular communication networks and internal regulatory signals by integrating intracellular and intercellular signaling. (1) CellCall collects ligand–receptor–transcription factor (L–R–TF) axis datasets based on KEGG pathways. (2) Using prior knowledge of L–R–TF interactions, CellCall infers intercellular communication by combining the expression of ligands/receptors and downstream transcription factor (TF) activity for specific L–R pairs. (3) CellCall incorporates a pathway activity analysis method to identify key pathways involved in communication between specific cell types. In this study, the R package CellCall [31] was used to analyze intercellular interactions involving 14 common ligand-receptor pairs across 8 cell types.

CellPhoneDB is a database that contains ligands, receptors, and their interactions, facilitating a comprehensive and systematic analysis of signaling molecules between cells, thereby enabling the study of intercellular communication and networks among different cell types [32].

The R software package CellChat [33] was utilized to import data from the CellPhoneDB database for the analysis of cellular communication from three main aspects: Secreted Signaling, ECM-receptor interactions, and cell–cell contact. The general workflow involves constructing CellChat objects using pre-existing scRNA-seq data, inferring the number of ligand–receptor pairs through the trimean method, calculating the communication probability of all ligand-receptor interactions related to each signaling pathway to assess the signaling pathway-level communication probability, visualizing each signaling pathway using hierarchical diagrams, circular plots, or chord diagrams, and prioritizing important signaling pathways based on inferred differences in internal information flow between two groups.

Analysis of differential gene expression

Differential analysis was performed on FOLR2+ macrophages between the Normal and Tumor groups using the R software package limma [34]. Genes with $|avg\_log2FC| > 0.5$ and $P < 0.05$ were selected as differentially expressed with a threshold. Additionally, FOLR2 expression was analyzed in healthy control breast tissue samples and BRCA patient tumor tissue samples based on TCGA and CPTAC datasets.

Gene function enrichment analysis

To further clarify the functional differences between FOLR2+ macrophages in the Normal and Tumor groups, the R package clusterProfiler [35] was employed. With a significance level set at $P < 0.05$, Gene Ontology (GO) enrichment analysis was conducted on the specific differentially expressed genes of FOLR2+ macrophages in the Normal and Tumor groups. The GO categories comprised biological processes (BP), cellular components (CC), and molecular function (MF) [36].

Prognostic analysis of single gene

This study assessed the prognostic significance of CXCL9 and CXCR3 in BRCA based on clinical data from the TCGA-BRCA dataset. Prognostic indicators, including OS, DSS, and PFI, were assessed. The proportional hazards assumption was tested using the survival package in R, followed by the development of survival regression models. Results were visualized with the R packages survminer and ggplot2. Statistical comparisons of OS, DSS, and PFI between high and low expression groups of CXCL9 and CXCR3 were conducted using the Log-rank test, with significance defined as $P < 0.05$ [37]. Furthermore, the correlation between FOLR2 mRNA and protein expression and OS in BRCA patients was examined using data from the METABRIC and CPTAC datasets.

Analysis of the TME

Utilizing the TCGA dataset, the analysis of the TME was conducted using the R software package "estimate". This involved the computation of StromalScore, ImmuneScore, and ESTIMATEScore for each sample. The subsequent step encompassed the examination of score discrepancies between the high and low-expression groups of FOLR2 [38].

Immune infiltration analysis

CIBERSORT is a deconvolution algorithm based on gene expression that describes the cellular composition of complex tissues. This method quantifies the abundance of specific cell types, which is validated by fluorescence-activated cell sorting (FACS). Gene expression data with standard annotations have been uploaded to the CIBERSORT portal, utilizing the LM22 signature and running the algorithm with 1000 permutations [39]. In this study, leveraging the TCGA dataset, CIBERSORT was utilized to calculate the relative proportions of 12 T cell subtypes in each sample, with 1000 simulation iterations and a significance threshold set at $P<0.05$. The analysis reveals differences in immune cell content between the high and low-expression groups of FOLR2 [40].

Correlation analysis

In this study, correlation analyses were conducted on the relationship between $CD8^+$ T cell content and FOLR2 expression, as well as cytotoxic cell content and FOLR2 expression using the corplot package in R software, based on data from TCGA [41, 42].

Reverse transcriptase-polymerase chain reaction (RT-qPCR)

RT-qPCR was employed to analyze the difference in FOLR2 mRNA expression between healthy control breast tissue samples and tumor tissue samples from BRCA patients. Total RNA was extracted using the Trizol reagent kit (10296010, Invitrogen, Thermo Fisher, USA), and RNA quality and concentration were assessed using UV–visible spectrophotometry (ND-1000, Nanodrop, Thermo Fisher, USA). Reverse transcription was performed using the PrimeScript™ RT-qPCR kit (RR086A, TaKaRa, Mountain View, CA, USA). Real-time quantitative RT-qPCR was carried out on the LightCycler 480 system (Roche Diagnostics, Pleasanton, CA, USA) using SYBR Premix Ex TaqTM (DRR820A, TaKaRa). GAPDH was used as the internal reference for mRNA. Primers for amplification were designed by Shanghai Youbio Company, and their sequences are provided in Table S2. The fold change in gene expression between the experimental and control groups was calculated using the $2^{-\Delta\Delta CT}$ method, where $\Delta\Delta CT = \Delta Ct$ experimental group $- \Delta Ct$ control group, and $\Delta Ct =$ target gene Ct $-$ reference gene Ct [43].

Western blot

Tissue and cellular total proteins were extracted using an efficient RIPA lysis buffer (R0010, Solarbio, Beijing, China) following the manufacturer's instructions. After lysis at 4 °C for 15 min and centrifugation at 15,000 rpm for 15 min, the supernatant was collected, and the protein concentration of each sample was determined using the BCA assay kit (20201ES76, Yisheng Biotechnology Co., Ltd., Shanghai, China). Quantification was performed based on different concentrations, and the proteins were separated by polyacrylamide gel electrophoresis. Subsequently, the proteins were transferred to a PVDF membrane using the wet transfer method, followed by blocking with 5% BSA at room temperature for 1 h. Diluted primary antibodies were added: FOLR2 (human: ab103998, 1:1000, Abcam, UK), CXCR3 (mouse: ab288437, 1:1000, Abcam, UK), β-actin (ab227387, 1:5000, Abcam, UK). The membrane was then incubated overnight at 4 °C, followed by washing with TBST three times for 5 min each. Subsequently, the membrane was treated with HRP-conjugated goat anti-rabbit IgG (ab205718, 1:20,000, Abcam, UK) at room temperature for 1 h. After washing with TBST three times for 5 min each, the membrane was developed using a substrate solution. Protein quantification analysis was performed using ImageJ 1.48 software (National Institutes of Health) by calculating the ratio of the grayscale values of each protein to the reference protein grayscale values, with β-actin (ab8226, 1:10,000, Abcam, UK) or Tubulin (ab7291, 1:10,000, Abcam, UK) used as internal controls. The experiment was repeated three times [44].

Immunohistochemical staining

Tumor tissues from humans or mice, as well as normal mammary gland tissues, were embedded in slices, baked at 60 °C for 20 min, sequentially placed in xylene solution, soaked for 15 min after changing xylene, immersed in anhydrous alcohol for 5 min, followed by another 5 min in anhydrous alcohol, then sequentially hydrated in 95% and 70% alcohol for 10 min each. Each slide was treated with 3% H_2O_2 at room temperature for 10 min to block endogenous peroxidase enzymes. Citrate buffer was added, microwaved for 3 min, antigen retrieval solution was dripped, left at room temperature for 10 min, and washed thrice with PBS. Normal goat serum blocking solution (E510009, Shanghai Sengong Bioengineering Co., Ltd.) was added at room temperature for 20 min, then diluted primary antibodies Ki67 (ab16667, 1:200, Abcam, UK) and FOLR2 (ab302532, 1:100, Abcam, UK)

were added separately and kept overnight at 4 °C, washed thrice with PBS, incubated with goat anti-rabbit IgG secondary antibody (ab6721, 1:1000, Abcam, UK) for 30 min, washed with PBS, and treated with DAB color development kit (DAB-M, Sigma-Aldrich, USA) by dripping solutions A, B, and C onto the specimen, followed by a 6-min color development, hematoxylin staining for 30 s, dehydration in 70%, 80%, 90%, 95% ethanol, and anhydrous ethanol for 2 min each, immersed in xylene for 5 min twice, and finally sealed with neutral resin. The slices were observed under a brightfield microscope (BX63, Olympus, Japan). The experiment was repeated three times. PBS was used instead of primary antibodies for incubation as a negative control. Five immunohistochemistry images from different fields of view were selected for quantitative analysis. The number of cells with brown staining signals in the cytoplasm in each field was counted as positive staining cells, the total number of cells in each field was recorded, and then the percentage of positive cells was calculated as follows: Percentage of positive cells = number of brown-stained cells/total number of cells × 100% [45].

Immunofluorescence staining

In this study, we performed confocal immunofluorescence co-localization of FOLR2+ macrophages, $CD31^+$ blood vessels, $CD206^+$ macrophages, or $CD8^+$ T cells in tumor tissues. Following tissue sectioning, antigen retrieval was conducted, and the tissue surrounding the designated area was delineated with a tissue pen. The sections were then immersed in a 3% hydrogen peroxide solution to block endogenous peroxidase, followed by blocking with serum or BSA. Specific primary antibodies were applied: rabbit anti-FOLR2 (ab302532, 1:50, Abcam, UK), rabbit anti-CD31 (ab76533, 1:500, Abcam, UK), CD206 (ab64693, 1:50, Abcam, UK), and rabbit anti-CD8 (ab237709, 1:100, Abcam, UK), and incubated overnight at 4°C. Subsequently, secondary antibodies conjugated with Alexa Fluor® 488, Alexa Fluor® 647, FITC, PerCP-Cy™5.5, or Cy3 were added for incubation [46].

For cell immunofluorescence, cells were washed with cold PBS and fixed with 4% paraformaldehyde (P885233, Macklin, Shanghai, China) for 15–30 min. Following this, cells were permeabilized with 0.1% Triton (L885651, Macklin, Shanghai, China) for 15 min to penetrate the cell membrane. After two washes with PBS, the cells were incubated in PBS containing 15% FBS overnight at 5°C and then incubated overnight at 4 °C with rabbit anti-FOLR2 (ab302532, 1:50, Abcam, UK), CD206 (ab64693, 1:50, Abcam, UK), and rabbit anti-CD8 (ab237709, 1:100, Abcam, UK) antibodies. Subsequently, the cells were incubated with secondary antibodies conjugated with Alexa Fluor® 568, Alexa Fluor® 488, Alexa Fluor® 647, and FITC for visualization under a fluorescence microscope (Zeiss Observer Z1, Germany) [47].

For immunofluorescence confocal imaging, $CD8^+$ T cells labeled with Carboxyfluorescein succinimidyl ester (CFSE) were injected intravenously into mice. Tumors were harvested 24 h post-injection and subjected to immunostaining. Frozen sections were stained with an anti-CD31 antibody (550274, BD Pharmingen) followed by a Cy3-conjugated secondary antibody (A10522, Life Technologies, USA). After PBS washing, sections were mounted with DAPI (Beyotime, Shanghai, China) and imaged at 200× magnification [48, 49].

Cell culture

$CD8^+$ T cells were isolated from the spleen and lymph nodes of a normal female C57BL/6 mouse (9–10 weeks old) using a Mouse $CD8^+$ T Cell Isolation Kit (70902-50, Beaverbio, Suzhou, China). The cells were stained with FITC-labeled anti-mouse CD8 antibody (ab237367, Abcam, UK) before and after sorting for flow cytometry analysis. The purity of $CD8^+$ T cells pre- and post-sorting was 13.8% and 97.1%, respectively, indicating successful isolation. The supernatant was collected by centrifugation at 3000×*g* for 10 min and filtered through a 0.2 μm filter [50]. The isolated $CD8^+$ T cells were stimulated with CD3/CD28 mouse activation beads (11452D, Thermo Fisher, USA) for 24 h prior to experimentation.

Tumor tissues from a mouse model of BRCA established in this study were processed using Mouse Tumor Tissue Macrophage Isolation Solution (xy1092MAC, ATCC). The macrophages were further classified as lineage-(CD3/CD19/NKP46/B220/Ly6G)$^-$Ly6C$^-$F4/80$^+$CD64$^+$FOLR2+ macrophages or lineage-(CD3/CD19/NKP46/B220/Ly6G)$^-$Ly6C$^-$F4/80$^+$CD64$^+$FOLR2$^-$ macrophages. Flow cytometry analysis was performed after staining with FITC-labeled anti-mouse FOLR2 antibody (ab234190, Abcam, UK), showing purities of 12.3% and 96.5% for FOLR2+ macrophages pre- and post-enrichment, respectively, indicating successful sorting.

The mouse BRCA cell line E0771 (Bio-53571, ATCC) was cultured in DMEM medium (11965092, Gibco, USA) supplemented with 10% FBS, 10 μg/mL streptomycin, and 100 U/mL penicillin. The cells were maintained at 37 °C with 5% CO_2 in a humidified incubator (Heracell™ Vios 160i CR CO_2 incubator, 51033770, Thermo Scientific™, Germany). The passage was performed when cells reached 80–90% confluency [49, 51, 52]. Co-culturing involved adding $CD8^+$ T cells to E0771 culture flasks at a 5:1 cell ratio, and the mixed cells were then co-incubated in a temperature-controlled chamber [53].

CRISPR/Cas9 gene editing technology

CRISPR/Cas9 technology was employed to create CXCL9-KO cells. The specific guide RNA sequences used were as follows: CXCL9-sgRNA Forward: 5′-TCC TTCAGCTGCTCCTGCTG-3′ (PAM sequence: AGG); Reverse: 5′-TGACAATAATAGTTTCAACA-3′ (PAM sequence: TGG). These sgRNA sequences were inserted into the Lenti-CRISPR v2 vector containing the Streptococcus pyogenes Cas9 nuclease gene (HanBio, Shanghai, China). Subsequently, cells were transduced with the lentiviral Lenti-CRISPR v2 vector, and the CRISPR/Cas9 editing system was applied to generate CXCL9-KO cells. The transfected cells, carrying sgRNA plasmids and donor sequences, were selected using 4 μg/mL puromycin (HY-K1057, MCE, USA). Surviving cells were then clonally expanded, and the CXCL9-KO cells were validated through RT-qPCR and Western blot analysis [54, 55].

Inhibition experiment on T cells

The antibody against CD3E (ab16669, Abcam, UK) was diluted to a concentration of 10 μg/ml in 1×PBS and allowed to incubate overnight at 4 °C or 37 °C. After incubation, the cells were washed once with 1×PBS. For the proliferation assay, purified $CD8^+$ T cells were labeled with 2 μM CFSE at 37 °C for 8 min. Subsequently, 50,000 macrophages were seeded at 100 μl/well in a 96-well plate coated with anti-CD3. In certain cases, recombinant TGFβ (100 ng/ml) (100-21C, Peprotech, USA) was added to the culture media for CFSE-labeled T cells. After co-culturing for 3 days, the T cells were stained for CD44 (CWA-1002, Sigma-Aldrich, USA), CD25 (CWA-1154, Sigma-Aldrich, USA), CD62L (CWA-1061, Sigma-Aldrich, USA), and PD-1 (MABC1132, Sigma-Aldrich, USA) to analyze their activation state. The CFSE dilution was also analyzed to assess T cell proliferation. Additionally, we directly treated $CD8^+$ T cells with CXCL9 and included anti-CXCR3 (SAB3501088, Sigma-Aldrich, USA) for rescue experiments. The staining procedures were repeated as described above to observe whether CXCL9 activates $CD8^+$ T cells through binding to CXCR3 [56].

T cell activation experiment

T cells were labeled with 2 μM CellTrace Violet (C34557, Invitrogen) at 37 °C for 20 min, washed, and then co-cultured with macrophages. A total of 25,000 macrophages were plated in a 96-well plate in a complete RPMI medium (10% FCS + 1% penicillin/streptomycin + 1 mM sodium pyruvate and 10 mM HEPES). Different doses of SIINFEKL OVA peptide (138831-86-4, Nanjing Peptide Bio, China) ranging from 0.1 to 100 nM were added and incubated with the macrophages at 37 °C for 45 min. After two washes, 25,000 CellTrace Violet (CTV)-labeled OTI $CD8^+$ T cells were added at a 1:1 ratio to the SIINFEKL-pulsed macrophages. After co-culturing for 3 days, T cells were stained for CD8 (47–0081-82, Sigma-Aldrich, USA), CD44 (CWA-1002, Sigma-Aldrich, USA), CD25 (CWA-1154, Sigma-Aldrich, USA), CD62L (CWA-1061, Sigma-Aldrich, USA), and PD-1 (MABC1132, Sigma-Aldrich, USA) to analyze their activation status. T cell proliferation was evaluated using the CTV dilution method. For intracellular cytokine detection, T cells were first surface-stained for CD8 for 30 min at 4 °C, followed by restimulation with phorbol 12-myristate 13-acetate (20 ng/ml; 524400, Sigma-Aldrich, USA), 1 μM ionomycin (I3909, Sigma-Aldrich, USA), and BD GolgiPlug in complete RPMI. After washing, cells were fixed with BD PermFix buffer for 20 min and then stained for CD8 on restimulated T cells. Intracellular staining for IFN-γ (FCMAB243P, Sigma-Aldrich, USA) and TNF-α (ab8097, Abcam, UK) was performed for 30 min in BD PermWash buffer [56].

Flow cytometry analysis

$CD3^+$ T cells isolated from mouse tumor tissues and spleens were stained with the following antibodies: APC-conjugated anti-CD8 (47–0081-82, Sigma-Aldrich, USA) and PE-conjugated anti-IFN-γ antibody for sorting IFN-γ + $CD8^+$ T cells. The cells were incubated for 30 min at 4 °C in the dark, followed by the addition of 2 mL PBS solution (P4417, Sigma-Aldrich, USA). After centrifugation for 10 min at 1500×*g* at 4 °C, the supernatant was discarded. The cells were fixed with 2% paraformaldehyde (30525-89-4, Sigma-Aldrich, USA)/PBS solution, stored at 4 °C in the dark, and analyzed within 24 h using the FACS Aria II flow cytometer (BD Bioscience, USA) [57].

Flow cytometry was utilized to assess the cell death rate. The general procedure involved collecting tumor cells (1×10^5/well), washing them in cold PBS, and staining them in the dark for 15 min using the test reagent kit (APOAF-20TST, Sigma-Aldrich, USA). Subsequently, the pellet was resuspended in 400 μL of binding buffer, and 5 μL of Annexin-V stain provided in the kit was added. Cell analysis was conducted using a flow cytometer [58]. Cells in the upper right quadrant with Annexin V^+PI^+ phenotype represented late apoptotic cells; cells in the lower right quadrant with Annexin V^+PI^- phenotype represented early apoptotic cells; cells in the upper left quadrant with Annexin V^-PI^+ phenotype represented necrotic cells, while cells in the lower left quadrant with Annexin V^-PI^- phenotype represented viable cells [59].

Cell viability assay using MTT

Cells were seeded at a density of 1×10^4 cells per well in a 96-well plate and incubated for 24 h. Subsequently, cells from different treatment groups were mixed with 0.01 mL of MTT solution (CT02, Sigma Aldrich, USA) and incubated in a CO_2 incubator for 4 h. Following incubation, 0.1 mL of isopropanol containing 0.04 N HCl was added to each well. The solution was thoroughly mixed using a multichannel pipette to ensure proper homogenization. HCl converted the phenol red in the culture medium to a yellow color that does not interfere with the MTT formazan measurement. Cell viability was determined by measuring the absorbance at 570 nm [60].

Multicellular spheroids (MCS) generation and 3D co-culture with $CD8^+$ T cells

To initiate the formation of MCS, 1000 cancer cells were seeded into 35- or 81-well agarose cylindrical molds (A6013, Sigma-Aldrich, USA) generated from 3D Petri dishes, which serve as the apparatus for MCS formation by Microtissues® Inc. (RI, USA). One minute post-seeding, 1 mL (for 35-well molds) or 2 mL (for 81-well molds) of cell culture medium was added, and the cells were incubated at 37°C and 5% CO_2 to allow for the formation of cancer spheroids. On the second day, CFSE-labeled $CD8^+$ T cells were added to the cancer spheroids at a 5:1 ratio, maintained in RPMI medium (R4130, Sigma-Aldrich, USA) supplemented with 10% fetal bovine serum and 100 units/mL penicillin/streptomycin, and co-cultured. After incubation at 37 °C for 24 h, the spheroids were washed and fixed in 4% paraformaldehyde. Imaging was performed using a ZEN 710 confocal microscope (ZEISS, Germany). Images were captured at the midpoint of the microsphere and surface maps were generated using Image J software.

Following a 2-day co-culture, invasion into Type I collagen (CC050, Sigma-Aldrich, USA) was initiated. Initially, the collagen was neutralized to a pH of 7.0–8.0, and the co-cultures were embedded in neutralized collagen within the agarose molds referred to earlier. After a 4-min incubation, the agarose molds containing the collagen-embedded co-cultures were inverted and further incubated for 1 h. Subsequently, the molds were reverted to their original position, and RPMI medium supplemented with 5% FBS and 1% penicillin/streptomycin was added. Invasion assays were conducted over 2 days, with imaging performed using an inverted microscope (XDS-900, Caikon, Shanghai, China) until images were captured and cells recovered from the collagen matrix were analyzed for viability.

For cytotoxicity assessment of $CD8^+$ T cells against tumor cells, the spheroids were washed 24 h post-co-culture, stained and fixed using a viability/cytotoxicity assay kit (30,002, Biotium, USA). Images were captured using a confocal microscope, with a Z-stack scanned at 5 μm intervals from the top to the middle of the MCS, then presented as maximum intensity projections. A surface display (2.5D) was obtained using Zeiss image processing software for quantitative analysis of live and dead cells, measuring the total cell area for each dye with Image J software [48, 61].

Enzyme-linked immunosorbent assay (ELISA)

The ELISA technique was employed to measure the concentrations of CXCL2, CXCL10, CXCL9, and CXCL13 in cellular supernatants, as well as the levels of IFN-γ in the mouse serum samples. The specific procedures were as follows: initially, antigens including IFN-γ (RAB0224, Sigma-Aldrich, USA), CXCL2 (ML058180, Shanghai Enzyme-linked Biotechnology Co., Ltd., China), CXCL10 (ML063284, Shanghai Enzyme-linked Biotechnology Co., Ltd., China), CXCL9 (ML037904, Shanghai Enzyme-linked Biotechnology Co., Ltd., China), and CXCL13 (LE-Y1253, Hefei Lail Biotechnology Co., Ltd., China) were diluted in coating buffer to appropriate concentrations and incubated in enzyme-labeled reaction wells at 37 °C for 40 min. Subsequently, 5% fetal bovine serum (F8318, Wuhan Merck Biotechnology Co., Ltd., China) was added. Next, the diluted samples were added to the enzyme-labeled reaction wells, followed by the addition of enzyme-linked antibodies and substrate solution. Finally, 50 μL of stop solution was added to each well to terminate the reaction. Experimental results were determined within 20 min, and the plates were read at 450 nm using an ELISA reader (Bio-Rad, USA) to generate a standard curve for data analysis [62].

$CXCR3^{-/-}$ specific knockout mouse model

The procurement process involved acquiring two mouse strains: Cxcr3-Flox (C57BL/6Smoc-Cxcr3em1(flox) Smoc, NM-CKO-2117369, Nanmo Biotech, China) and Pbsn-2A-CreERT2 transgenic mice (C57BL/6JSmoc-Pbsnem1(V5-2A-CreERT2-WPRE-polyA)Smoc, NM-KI-200190, Nanmo Biotech, China). These strains were then bred in the laboratory to generate mice with a specific homozygous deletion of CXCR3 in the mammary glands, spleen, and lymph nodes, resulting in $CXCR3^{-/-}$ mice. Validation of $CXCR3^{-/-}$ female mice was conducted using RT-qPCR and Western Blot to confirm the mRNA and protein expression levels of CXCR3 in mammary glands, spleen, and lymph node tissues obtained from these mice, ensuring the successful establishment of the $CXCR3^{-/-}$ mouse model [63].

BRCA in situ transplantation model and animal grouping

We purchased 60 female C57BL/6 mice, aged 6 weeks and weighing 16–20 g, from our institution's animal research center. All mouse experiments complied with the animal care policies of the China Food and Drug Administration (SFDA). The animals were all treated with humane care standards outlined in the "Guide for the Care and Use of Laboratory Animals" published by the National Academy of Sciences of the United States and the National Institutes of Health. The mice were housed in sterile cages with sterile food and water, maintained under sterile conditions throughout the experiment, with room temperature kept between 24 and 26 °C and humidity controlled at 40–60%.

To establish a BRCA in situ transplantation model, we subcutaneously injected E0771 cells (2×10^6) into the right inguinal mammary fat pad of 6-week-old mice. Tumor volumes were measured every 3 days using a digital caliper, calculated using the formula tumor volume (mm^3) = $d^2\times D/2$, where d is the smallest diameter, and D is the largest diameter. After 24 days, mice were euthanized under general anesthesia, then killed by cervical dislocation, and tumors were excised for further experimental analysis by processing them with FFPE (Formalin-Fixed Paraffin-Embedded) or rapid freezing [64].

Furthermore, for the in situ transplantation tumor model constructed in CXCR3 gene knockout ($CXCR3^{-/-}$) mice and wild-type (WT) control mice, FOLR2-macrophages or FOLR2+ macrophages (1×10^7) cultured and labeled with CFSE were injected into the tumors. The mice's tumor growth was observed, and the activation status of $CD8^+$ T cells was assessed using flow cytometry and ELISA [56].

Real-time in vivo near-infrared fluorescence imaging

Near-infrared imaging was utilized for the quantitative localization of $CD8^+$ T cells dynamically within the murine body. $CD8^+$ T cells were treated directly with 100 ng/ml of CXCL9 (ab50083, Abcam, UK) for the CXCL9 group, while the Control group was treated with an equal volume of DMSO. The $CD8^+$ T cells were divided into four groups: CXCR3-WT Control group, CXCR3-WT CXCL9 group, CXCR3-KO Control group, and CXCR3-KO CXCL9 group. Subsequently, the $CD8^+$ T cells were labeled with the near-infrared fluorescent probe DiR (MX4005, Meikon Biotechnology, Shanghai, China) at 1 μM, and co-incubated with the cells at 37 °C for 20 min. The labeled $CD8^+$ T cells (1×10^7) were then suspended in 200 μL of PBS and injected through the tail vein or directly into the tumor of mice transplanted with tumors for 12 or 36 days. Anesthetization and scanning of the mice were conducted using the CRi Maestro in vivo imaging system (Cambridge Research and Instrumentation, Massachusetts, USA). For ex vivo tissue imaging, mice were euthanized by deep anesthesia using isoflurane (R510-22-10, RWD Life Science, Shenzhen, China) followed by cervical dislocation. Tumors and major organs, including the heart, liver, spleen, lungs, kidneys, and intestines, were excised for analysis [48, 65, 65].

Statistical analysis

Our study utilized version 4.2.1 of the R programming language, with compilation carried out using the RStudio integrated development environment (version 2022.12.0–353). GraphPad Prism 8.0 software was used for statistical analysis. Descriptive statistics were presented as mean ± standard deviation (Mean ± SD). The comparison between two groups of data was conducted using a two-sample t-test, whereas multiple group comparisons were assessed using a one-way analysis of variance (ANOVA). The homogeneity of variance was examined using Levene's test. In cases of homoscedasticity, pairwise comparisons were conducted using Dunnett's T3 and LSD t-tests, while Dunnett's T3 test was applied in cases of heteroscedasticity. A significance level of $P<0.05$ was considered as indicative of statistically significant differences between the compared data sets [66].

Results

Identification of 8 cell subpopulations in tumor tissues of BRCA patients using scRNA-seq

To establish a comprehensive single-cell transcriptomic map of tumor tissues in BRCA patients, we collected samples from 4 normal breast tissues (N1–4) and 4 BRCA tumor tissues (T1–4) for scRNA-seq (Fig. 1A).

(See figure on next page.)

Fig. 1 Single-cell atlas of healthy control breast tissue samples and BRCA patient tumor tissue samples. *Note* **A** Schematic representation of the single-cell sequencing workflow; **B** UMAP analysis clustering all cells into 14 cell clusters, where each color represents a cluster; **C** Annotation of the 14 cell clusters into 8 major cell types based on the expression of known marker genes; **D** Dot plot showing the expression of marker genes in each cell cluster; **E** CNV analysis of scRNA-seq data; "Reference" represents NKT cells, with yellow indicating reference NKT cells and cyan indicating epithelial cells. In the map, blue represents DNA copy loss, and red represents DNA copy gain; **F** CNV scores after K-means clustering; **G** UMAP plot of scRNA-seq data after extraction of malignant cells; **H** Bar graph illustrating the proportions of different cell types in BRCA patient tumor tissue samples (Normal group, n = 4) and healthy control breast tissue samples (Tumor group, n = 4), with *indicating $P<0.05$

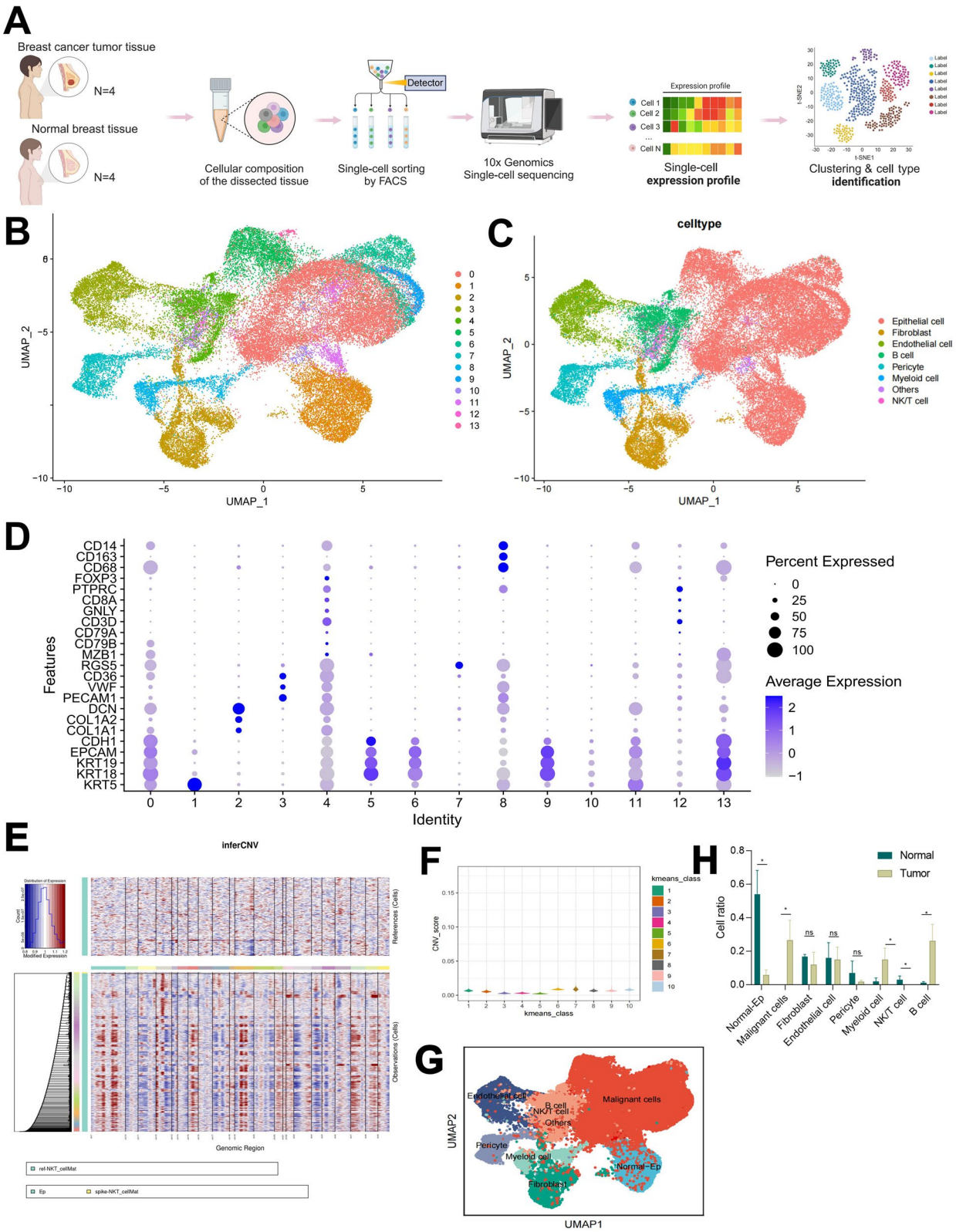

Fig. 1 (See legend on previous page.)

Initially, we performed quality control and normalization using the R package Seurat, filtering out low-quality cells based on criteria including expression of genes per cell (nFeature_RNA) > 200, detected RNA molecules per cell (nCount_RNA) < 5000, and the percentage of mitochondrial genes (percent.mt) < 15. Subsequently, 25,499 cells from the Normal group and 21,022 cells from the Tumor group passed quality control (Fig. S1A–D). Correlation analysis of post-filtered data revealed r values of 0.01 and −0.02 between nCount_RNA and percent.mt, and 0.93 and 0.89 between nCount_RNA and nFeature_RNA (Fig. S1B–E), indicating high data quality. Identification of highly variable genes from the filtered cells resulted in the selection of the top 2000 genes for downstream analysis (Fig. S1C–F).

Next, batch-corrected integration of all samples was performed, followed by PCA of the top 2000 highly variable genes using the RunPCA function. The DimHeatmap function was utilized to visualize the heat map of the first 2 principal components (Fig. S2A) and display the key genes contributing to these components (Fig. S2B). Visual inspection with the JackStrawPlot function revealed that the *P* values of the first 50 principal components were typically small, indicating their importance in capturing information from the highly variable genes selected earlier. In particular, the *P* values of the first 10 principal components were all below 0.05 (Fig. S2C). Further analysis with the ElbowPlot function showed an inflection point in the standard deviation at the 10th principal component (Fig. S2D), suggesting that these components effectively encapsulate the information from the selected highly variable genes. Consequently, we proceeded with UMAP clustering analysis using these 10 principal components.

Subsequently, the UMAP algorithm was applied to perform non-linear dimensionality reduction on the top 10 principal components, clustering all cells into 14 cell clusters (Fig. 1B). Based on cell marker genes, the clusters were ultimately annotated into 8 major cell types: Epithelial cells (markers: KRT5, KRT18, KRT19, EPCAM, CDH1), Fibroblasts (markers: COL1A1, COL1A2, DCN), Endothelial cells (markers: PECAM1, VWF, CD36), B cells (markers: MZB1, CD79B, CD79A), Pericytes (marker: RGS5), Myeloid cells (markers: CD68, CD163, CD14), and NK/T cells (markers: CD3D, GNLY, CD8A, PTPRC, FOXP3). Cells that could not be annotated were categorized as "Others", which may represent rare cell types, states of differentiation or transformation, or blood cells (Fig. 1C, D).

To investigate the changes in the aforementioned cell types in breast cancer samples, we used NKT cells as a control and employed the "inferCNV" package to extract malignant cells by detecting large-scale copy number variations (CNV). The results showed that most of the epithelial cells in the three epithelial cell types underwent CNV (Fig. 1E).

Subsequently, we clustered the normal and malignant cells in the "Observation" dataset, and the results revealed that Classes 3, 4, and 5 predominantly contained normal epithelial cells (Normal-Ep) with the lowest CNV scores. In contrast, Classes 1, 2, 6, 7, 8, 9, and 10 corresponded to malignant cells, which exhibited the highest CNV scores (Fig. 1F). We further updated the cell annotation (Fig. 1G) and displayed the changes in the proportions of various cell types between healthy control breast tissue samples and breast cancer tumor samples. From Fig. 1H, we can observe significant changes between the Normal and Tumor groups in the proportions of Normal-Ep, Malignant cells, and immune cells (B cells, Myeloid cells, and NK/T cells). However, there were no significant differences between the two groups in the proportions of Fibroblasts, Endothelial cells, and Pericytes. Existing evidence indicates that changes in the quantity and function of local and systemic immune cells drive the severity of breast cancer [67]. Therefore, our subsequent focus will be on exploring the specific mechanisms by which immune cells exert their roles in the tumor tissues of breast cancer patients.

In summary, we have constructed a single-cell transcriptomic atlas comprising 46,521 cells through scRNA-seq. Notably, there are substantial changes in the content of immune cells between healthy control breast tissue samples and BRCA patient tumor tissue samples, suggesting a potentially pivotal role in the disease progression of BRCA patients.

Close communication between FOLR2+ macrophages and CD8$^+$ T cells in tumor tissue samples of BRCA patients

First, we re-clustered all immune cells into 16 clusters (Fig. 2A). After removing low-quality cells (cluster 0, 2, and 13), we annotated the remaining cells into 8 types of immune cells based on cell marker genes: B cells (markers: MZB1, CD79B, CD79A), CD4$^+$ T cells (markers: CD4, FOXP3), CD8$^+$ T cells (markers: CD8A, CD3D, PTPRC, GNLY), Mast cells (marker: KIT), Dendritic cells (markers: IRF7, TCF4), and Macrophages (markers: CD14, CD68, CD163, C1QA, C1QB, C1QC) (Fig. 2B–D). Macrophages were further classified into FOLR2+ macrophages, TREM2$^+$ macrophages, and CCR7$^+$ macrophages (Fig. 2E). Additionally, we analyzed the expression levels of PD-L1 (CD274) in immune cells and found no significant differences (Fig. 2F).

To further elucidate the roles of various immune cells in the BRCA tumor immune microenvironment, we conducted cellular communication analysis on scRNA-seq data from both healthy control breast tissue samples and

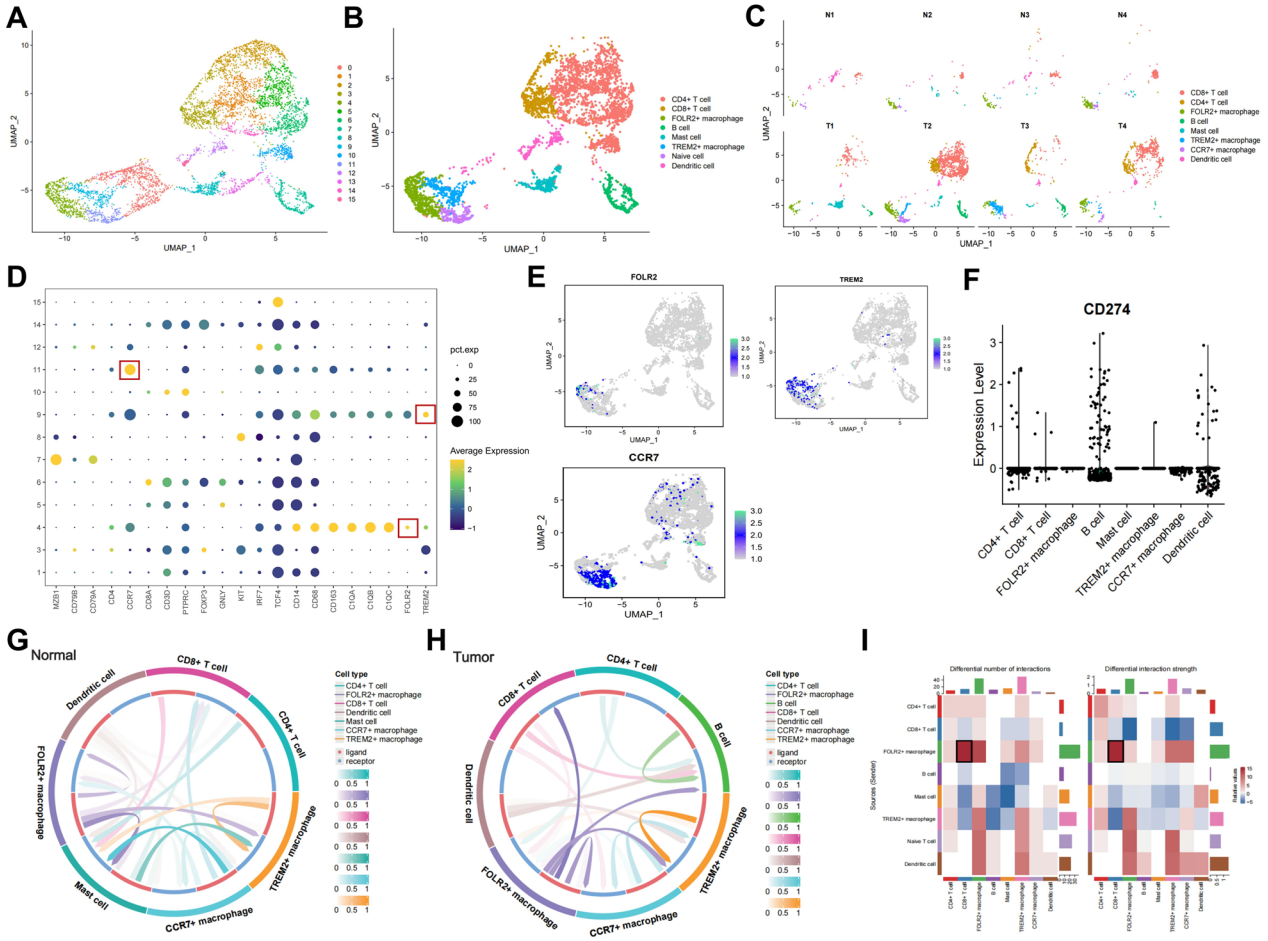

Fig. 2 Immune cell annotation and cellular communication in healthy control breast tissue samples and BRCA patient tumor tissue samples. *Note* **A** UMAP analysis classified all immune cells into 16 cell clusters, with each color representing a cluster; **B** Annotation of the 16 cell clusters into 8 classes of immune cells based on the expression of known marker genes; **C** The distribution of eight immune cell types within each sample; **D** Dot plots displaying the expression of marker genes in each cell cluster; **E** Distribution of FOLR2, TREM2 and CCR7 among different cell types; **F** Distribution of CD274 among different cell types; **G** and **H** Results of the R software package cellcall analysis, depicting cellular communication in healthy control breast tissue samples (Normal group, n = 4) and BRCA patient tumor tissue samples (Tumor group, n = 4), where darker arrow colors indicate a higher degree of receptor-ligand binding; **I** Results of the R software package cellchat analysis, with red squares indicating more frequent and stronger interactions in the Tumor group, and blue squares indicating fewer and weaker interactions in the Tumor group

tumor tissue samples of BRCA patients. Cellular communication analysis is based on ligand-receptor pairs expressed between two cell types, reflecting cellular communication relationships through molecular interactions. Initially, we used the R software package CellCall to analyze 14 common ligand-receptor interactions between the 8 cell types. The results revealed significant cellular interactions between Mast cells, TREM2+ macrophages, and other cells in the Normal group, while the Tumor group showed a marked increase in interactions involving FOLR2+ macrophages, primarily acting as ligand cells. Notably, the interaction between FOLR2+ macrophages and $CD8^+$ T cells was particularly significant (Fig. 2G, H).

In this study, we utilized the R software package CellChat to import data from the CellPhoneDB database and analyze the differences in cellular communication between samples of healthy control breast tissue and BRCA tumor tissue. The CellChatDB in humans comprises 1939 validated molecular interactions, including 61.8% for Secreted Signaling interactions, 21.7% for extracellular matrix-receptor (ECM-Receptor) interactions, and 16.5% for Cell–Cell Contact interactions. In the Secreted Signaling aspect, a comparison was made between the total number and intensity (weight) of cell interactions in the two groups, revealing that the tumor group exhibited significantly closer cell connections, with the cell interaction frequency approximately four times

higher in the tumor group than in the normal group (Fig. S3A). Furthermore, using circle plots and heatmaps, we visually demonstrated the changes in cellular communication occurring in the tumor group compared to the normal group, with red indicating upregulation and blue downregulation. The results showed that the tumor group had a greater total number of cell interactions and higher interaction intensities, particularly evident in the increased closeness and frequency of interaction between FOLR2+ macrophages and $CD8^+$ T cells (Figs. S3B and 2I). Conversely, in terms of ECM-Receptor and Cell–Cell Contact interactions, there were no significant differences in the total number of cell interactions between the tumor and normal groups (Fig. S3C–F), suggesting that cellular communication in BRCA tumor tissue samples predominantly occurs via Secreted Signaling.

These findings collectively indicate that the analyses from the R software packages CellCall and CellChat are consistent and both confirm significant alterations in the total number and intensity of cell interactions in BRCA tumor tissue samples compared to healthy control breast tissue samples, primarily emphasizing changes in Secreted Signaling. The enhanced communication between FOLR2+ macrophages and $CD8^+$ T cells in BRCA tumor tissue samples may play a crucial role in the immune microenvironment of BRCA tumors.

High expression of FOLR2 and high density of FOLR2+ macrophages are positively correlated with a good prognosis in BRCA patients

An analysis of the TCGA-BRCA dataset was conducted to compare the differential expression of FOLR2 in samples of healthy control breast tissue and tumor tissue from BRCA patients. The results indicate a significant decrease in mRNA expression levels of FOLR2 in the Tumor group compared to the Normal group (Fig. S4A). Further analysis from the CPTAC database revealed a significant decrease in protein expression levels of FOLR2 in the Tumor group compared to the Normal group (Fig. S4B). Subsequently, we collected 117 samples of tumor tissue from BRCA patients and 43 samples of normal breast tissue from our institution and validated the differential expression of FOLR2 through RT-qPCR and Western blot. It was found that both mRNA and protein expression levels of FOLR2 were significantly decreased in the tumor tissue of BRCA patients (Fig. S4C, D). These results suggest a significant downregulation of FOLR2 expression in tumor tissue of BRCA patients compared to normal control breast tissue.

To explore the role of FOLR2+ macrophages in BRCA, immunofluorescence staining was performed to label FOLR2 and the macrophage marker CD206, as well as CD31, to identify blood vessels. The results indicate that FOLR2+ CD206 + macrophages are predominantly located near CD31-marked blood vessels, indicating their potential involvement in regulating tumor vasculature and immune response (Fig. S4E). Furthermore, analysis from the TCGA-BRCA dataset also showed a negative correlation between FOLR2 expression and the T stage of tumors (Fig. S4F), and ROC curve analysis demonstrated the favorable prognostic diagnostic effect of FOLR2 (Fig. S4G), consistent with the findings of Wang et al. [68].

To directly assess the correlation between the cell density of FOLR2+ macrophages and clinical outcomes, we conducted staining of tumor tissue for FOLR2, the macrophage marker CD206, and 4′,6-diamidino-2-phenylindole (DAPI). The results revealed a positive correlation between the density of FOLR2+ macrophages in BRCA tissue and their expression levels of FOLR2 (Figure S4H). By setting the optimal performance threshold as the critical value, it was observed that the density of FOLR2+ macrophages is positively associated with patient survival (Fig. S4I, J). From these findings, it is suggested that FOLR2 and FOLR2+ macrophages hold considerable value for prognostic evaluation in BRCA patients.

Enrichment of FOLR2+ macrophages in tumor tissue of BRCA patients with $CD8^+$ T cell infiltration

We utilized the R software package "estimate" to calculate stromal and immune scores for each tumor tissue sample of BRCA patients. Subsequently, we analyzed the correlation of FOLR2 expression with these scores, revealing a positive association between FOLR2 expression and StromalScore, ImmuneScore, and ESTIMATEScore (Fig. S5A). Further, employing the ssGSEA algorithm to compute the proportion of T cell immune infiltration, differential analysis results indicated that compared to the low FOLR2 expression group, the high FOLR2 expression group exhibited significantly higher proportions of $CD8^+$ T cells and cytotoxic cells infiltration (Fig. S5B). Correlation analysis demonstrated a significant positive relationship between FOLR2 expression and the proportions of $CD8^+$ T cells, cytotoxic cells, and other cell infiltrates (Fig. S5C–E). These findings suggest a close association between FOLR2 and T cell immune infiltration in the TME of BRCA patients, particularly with $CD8^+$ T cells.

Observing tumor resection samples using confocal microscopy, we observed a close association between FOLR2+ macrophages located near CD31+ blood vessels and aggregates of $CD8^+$ T cells (Fig. 3A). To verify the spatial relationship between FOLR2+ macrophages and $CD8^+$ T cells, we performed cell staining on a tissue microarray patient cohort for $CD8^+$ and FOLR2+ cells and calculated their respective cell densities. The

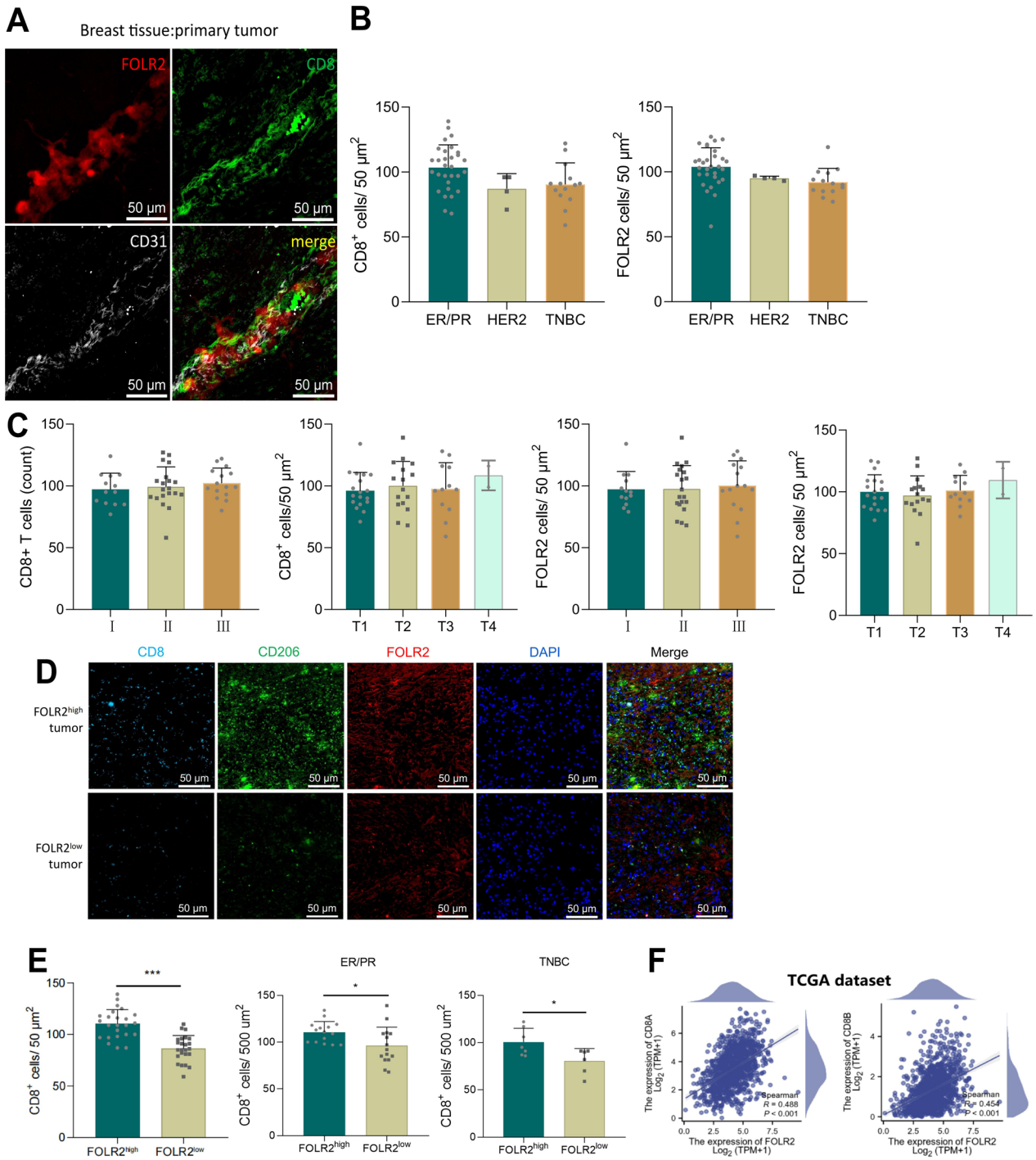

Fig. 3 Distribution of FOLR2+ macrophages and CD8$^+$ T cells in tumor tissue of BRCA patients. *Note* **A** Representative co-localization confocal immunofluorescence image of FOLR2+ macrophages, CD31+ blood vessels, and CD8$^+$ T cells in primary BRCA tumor tissue (Scale bars = 50 μm); **B** Stratification of CD8$^+$ T cells and FOLR2+ macrophages based on subtype using multiplex immunofluorescence quantification; **C** Stratification of patients based on tumor staging using multiplex immunofluorescence quantification of FOLR2+ macrophages; **D** Representative multiplex immunofluorescence image showing expression of CD8, FOLR2, and CD206 proteins (Scale bars = 50 μm); **E** Quantitative analysis of CD8$^+$ T cell density; **F** Analysis of the correlation between FOLR2 expression and CD8A, CD8B expression using the TCGA-BRCA dataset (n = 1113). ***indicates $P < 0.001$

density of FOLR2+ and CD8$^+$ T cells showed no significant differences between BRCA subtypes or tumor stages (Fig. 3B, C). However, tumors with a high content of FOLR2+ macrophages showed significantly higher CD8$^+$ T cell density compared to tumors with low FOLR2+ macrophage content. The same results were observed in both ER/PR-positive and TNBC subtypes (statistical analysis could not be performed for HER2 due to the small sample size) (Fig. 3D, E). This indicates that FOLR2+ macrophages are a structural component of lymphoid aggregates near tumor nests and are enriched in tumor tissue of BRCA patients with CD8$^+$ T cell infiltration.

Moreover, analysis of the TCGA dataset revealed a significant positive correlation between FOLR2 and the expression of CD8A and CD8B (Fig. 3F). In summary, there may be an interaction between FOLR2+ macrophages and CD8$^+$ T cells in the TME of BRCA patients, potentially influencing their immune infiltration.

FOLR2+ macrophages likely play a crucial role in antitumor immunity by modulating CD8$^+$ T cell function through the CXCL9-CXCR3 pathway

Based on scRNA-seq data, we conducted differential analysis on FOLR2+ macrophages in the Normal and Tumor groups. Using a threshold of $|avg\_log2FC| > 0.5$ and $adjP < 0.05$, a total of 79 significantly downregulated genes were identified in Tumor group FOLR2+ macrophages, along with 117 significantly upregulated genes. Among these genes, FOLR2+ macrophages in the Tumor group exhibited expression of genes involved in immune system processes, such as B cell and T cell chemokines (CCL7, CXCL2, CXCL10, CXCL9, CXCR4, CXCL13), adhesion molecule ICAM1, and lysosomal protein RAB32, while the Normal group FOLR2+ macrophages were enriched in genes regulating metabolic processes (LPL, FABP4, IGF1) (Fig. 4A). Subsequent functional enrichment analysis of the differentially expressed genes confirmed changes in functions and components related to long-chain fatty acid binding, CXCR chemokine receptor binding, and cytokine activity in the Tumor group (Fig. 4B–D). These findings suggest that FOLR2+ macrophages may play a crucial role in antitumor immunity, potentially affecting CD8$^+$ T cell function through pathways involving CXCR chemokine receptor binding and cytokine activity.

To clarify the specific pathway through which FOLR2+ macrophages act on CD8$^+$ T cells, we analyzed cellular communication pathways in the Tumor group using the R software packages CellCall and CellChat. Interestingly, as shown in Fig. S6A and B, the CXCL9-CXCR3 pathway exhibited strong interaction strength in both analyses, suggesting that ligands from FOLR2+ macrophages may bind to the CXCR3 receptor via the CXCL9 pathway, thereby influencing the function of CD8$^+$ T cells. Survival analysis based on the TCGA-BRCA dataset revealed that BRCA patients with high CXCL9 expression had better overall survival (OS) and PFI, while no significant difference was observed in DSS (Fig. S7A–C). Additionally, patients with high CXCR3 expression showed improved OS, DSS, and PFI (Fig. S7D–F).

In summary, FOLR2+ macrophages may play a crucial role in antitumor immunity in BRCA by influencing CD8$^+$ T cell function through the CXCL9-CXCR3 pathway.

FOLR2+ macrophages activate CD8.$^+$ T cell function primarily through secretion of CXCL9 to bind CXCR3

To directly assess the ability of FOLR2+ macrophages to activate CD8$^+$ T cells, we isolated FOLR2+ and FOLR2− macrophages from tumor tissues of BRCA mice (Fig. S8). Initially, we distinguished live cells from dead cells using DAPI staining and identified all immune cells by selecting CD45 positivity. Subsequently, specific immune cell subsets were excluded using antibodies against the linear (Lin) cell markers (such as Ly6G). By further identifying macrophages with MHCII and F4/80 as markers and refining TAMs subsets with the co-expression of FOLR2 and CADM1 (Fig. S5), we co-cultured FOLR2+ macrophages with CD8$^+$ T cells, followed by T cell suppression and antigen-specific T cell activation assays.

In the T cell suppression assay, purified FOLR2+ macrophages were co-cultured with polyclonally activated CD8$^+$ T cells. We observed that FOLR2+ macrophages not only failed to suppress T cell proliferation but instead promoted it, as evidenced by CFSE dilution. Additionally, FOLR2+ macrophages enhanced the proportion of CD25+ (activated) and CD62L− (circulating memory) double-positive T cells (T_eff), indicating enhanced T cell differentiation (Fig. 5A). Subsequently, in the antigen-specific T cell activation assay, purified FOLR2+ macrophages loaded with the OTI-specific SIINFEKL peptide were washed and co-cultured with OTI CD8$^+$ T cells. We found that compared to FOLR2− macrophages, FOLR2+ macrophages effectively activated OTI CD8$^+$ T cells, demonstrating superior induction of naive T cell activation (Fig. 5B) as well as enhanced proliferation of cells expressing IFN-γ and TNF-α, leading to increased multifunctionality (Fig. 5C). In conclusion, the evidence presented indicates that the behavior of FOLR2+ macrophages does not resemble that of immunosuppressive cells. Instead, FOLR2+ macrophages function as efficient antigen-presenting cells, displaying the capability to activate CD8$^+$ T cells.

Do FOLR2+ macrophages activate CD8$^+$ T cell function through secretion of CXCL9 to bind CXCR3?

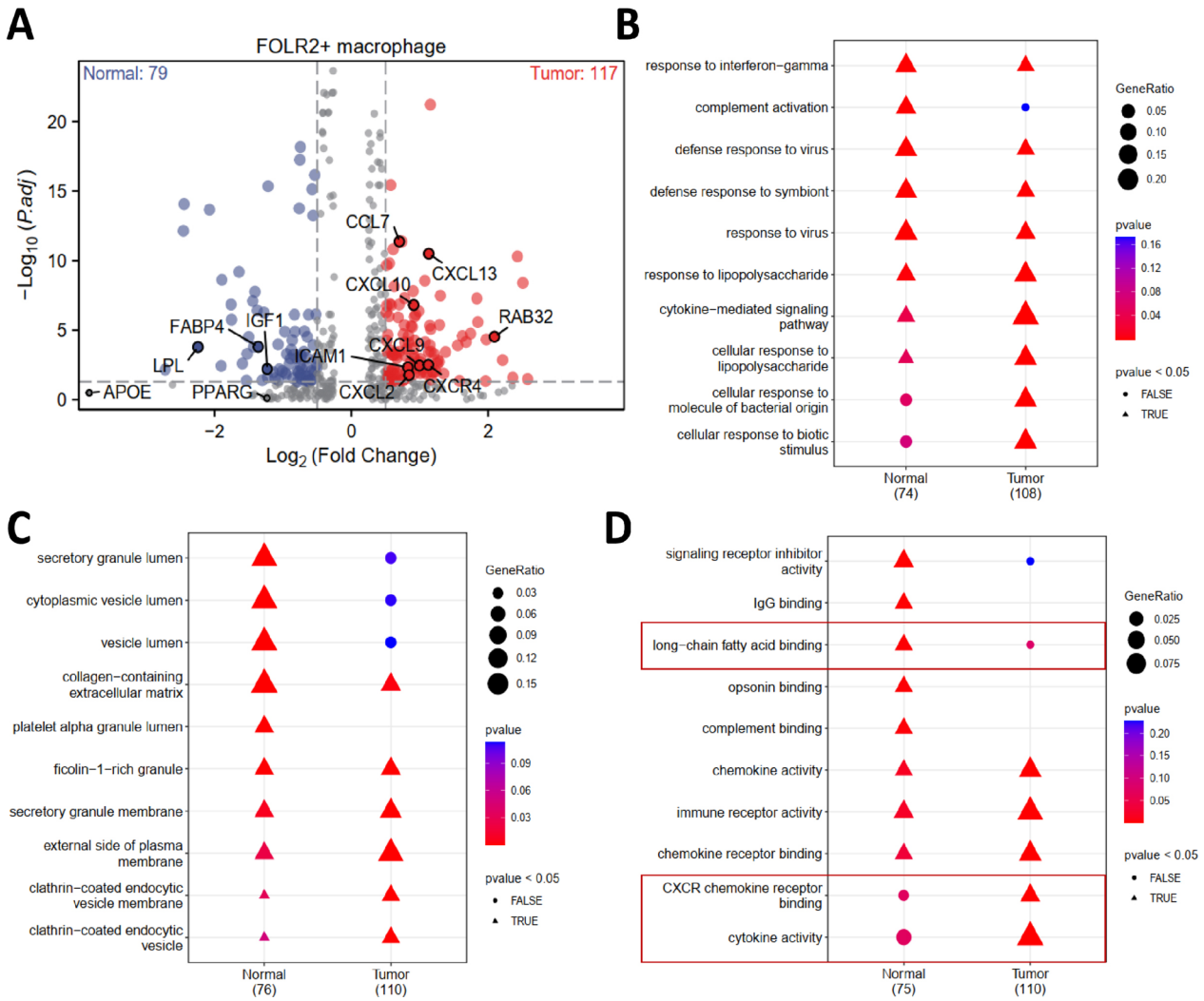

Fig. 4 Functional enrichment analysis of differentially expressed genes between FOLR2+ macrophages in healthy control breast tissue and tumor tissue samples from BRCA patients. *Note* **A** Volcano plot showing differentially expressed genes between FOLR2+ macrophages in normal breast tissue samples (Normal group, n = 4) and tumor tissue samples from BRCA patients (Tumor group, n = 4); blue points to the left of the dashed line represent genes significantly downregulated in the Tumor group, while red points to the right indicate genes significantly upregulated in the Tumor group; **B**–**D** Enrichment analysis of GO for differentially expressed genes between FOLR2+ macrophages in Normal and Tumor groups, including BP, CC, and MF

Considering previous results showing high expression of CXCL2, CXCL10, CXCL9, and CXCL13 in FOLR2+ macrophages in tumor tissues of BRCA patients, we collected cell culture supernatants from FOLR2− and FOLR2+ macrophages isolated from BRCA mouse tumor tissues and assessed the levels of CXCL2, CXCL10, CXCL9, and CXCL13 by ELISA. The results indicated a significant upregulation of only CXCL9 in FOLR2+ macrophages from the Tumor group compared to the FOLR2− macrophages group (Fig. 5D). Subsequently, treating $CD8^+$ T cells with CXCL9 and adding anti-CXCR3 for rescue experiments revealed that CXCL9 activated $CD8^+$ T cells through binding to CXCR3. The results of the antigen-specific T cell activation assay showed a significant expansion and activation of $CD8^+$ T cells after CXCL9 treatment, whereas the addition of anti-CXCR3 resulted in a marked reduction in $CD8^+$ T cell numbers, indicating suppression of their function (Fig. 5E, F). These findings collectively suggest that FOLR2+ macrophages primarily activate $CD8^+$ T cell function through secretion of CXCL9 to bind CXCR3.

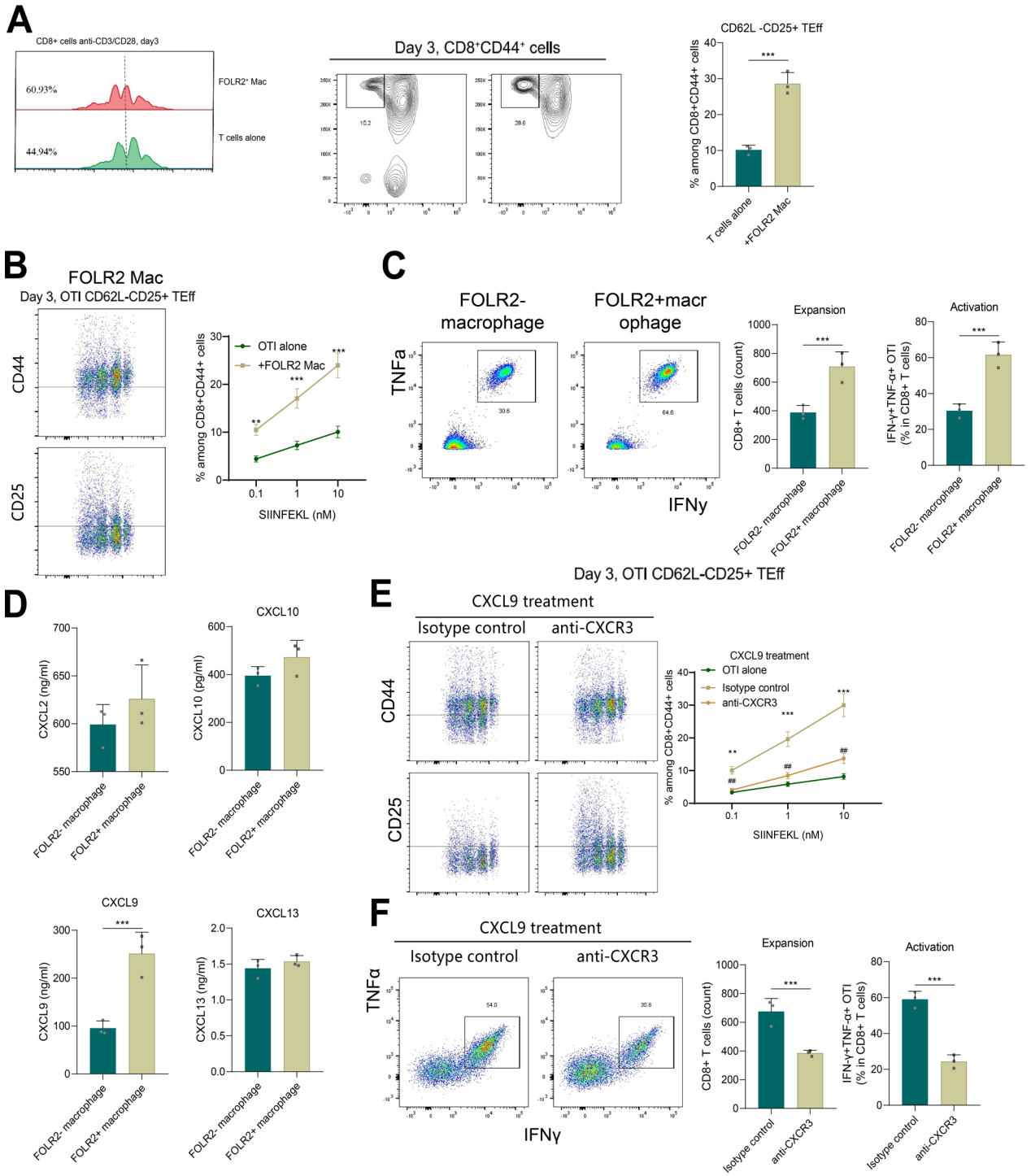

Fig. 5 Mechanistic investigation of FOLR2+ macrophage-mediated activation of $CD8^+$ T cells. *Note* **A** Evaluation of T cell proliferation and activation by flow cytometry 3 days post-induction, representative histograms displaying individual T cells, TGF-β, and co-culture with FOLR2+ macrophages for CFSE dilution, flow cytometry showing expression of CD25 and CD62L in effector $CD8^+CD44^+$ T cells; **B** and **C** Co-culturing of SIINFEKL OVA peptide-pulsed FOLR2+ macrophages with CTV-labeled naive OTI $CD8^+$ T cells, where Figure **B** represents evaluation of T cell proliferation and activation by flow cytometry 3 days post-induction, and Figure C displays flow cytometry analysis of $CD8^+$ T cell quantity, along with the percentage of TNF-α and IFN-γ positive cells; **D** ELISA measurement of CXCL2, CXCL10, CXCL9, and CXCL13 levels in cell culture supernatant; **E** Evaluation of T cell proliferation and activation by flow cytometry; **F** Flow cytometry assessment of $CD8^+$ T cell quantity and the percentage of TNF-α and IFN-γ positive cells; ***indicates $P < 0.001$, cell experiments were repeated three times

The CXCL9-CXCR3 axis regulates CD8$^+$ T cell infiltration functionalities impacting tumor cell growth, invasion, and survival

Our study revealed that FOLR2+ macrophages primarily activate CD8$^+$ T cell functionality through the secretion of CXCL9, which binds to CXCR3. Subsequently, we further validated the influence of the CXCL9-CXCR3 axis on CD8 + T cell functionalities and BRCA cell growth, invasion, and survival.

CD8$^+$ T cells isolated from normal mouse spleens and lymph nodes were genetically edited using CRISPR/Cas9 technology to knockout CXCR3 (Fig. S9A, B). Subsequently, different groups of CD8$^+$ T cells were treated with CXCL9. Co-culturing these CD8$^+$ T cell groups with the E0771 BRCA cell line, we assessed tumor cell proliferation using a CCK-8 assay and detected cellular apoptosis by flow cytometry. The results indicate that in the CXCR3-WT group, CXCL9 significantly inhibited tumor cell proliferation and increased apoptosis, while CXCR3 knockout enhanced proliferation and reduced apoptosis. Conversely, CXCL9 had no significant impact on tumor cell proliferation and apoptosis in the CXCR3-KO group (Fig. 6A, B). These results suggest that knocking out CXCR3 can reverse the effects of CXCL9 on tumor cell proliferation and apoptosis, highlighting the critical role of the CXCL9-CXCR3 axis in influencing tumor cell growth and apoptosis through CD8$^+$ T cells.

To better mimic the in vivo environment, we first constructed 3D cancer spheroids of the E0771 cell line and co-cultured them with CFSE-labeled CD8$^+$ T cells. Results showed that in the CXCR3-WT group, CXCL9 treatment significantly increased the infiltration rate of CD8$^+$ T cells, while CXCR3 knockout decreased the infiltration rate. Conversely, CXCL9 had no significant effect on the infiltration rate of CD8$^+$ T cells in the CXCR3-KO group (Fig. 6C), indicating the significant impact of the CXCL9-CXCR3 axis on the infiltration capability of CD8$^+$ T cells. Furthermore, we assessed the influence of different groups of CD8$^+$ T cells on the invasive ability of BRCA cells. After co-culturing for 4 days, the results demonstrated that in the CXCR3-WT group, CXCL9-treated CD8$^+$ T cells significantly reduced the invasive spread of spheroids, while CXCR3 knockout led to a significant increase in invasive spread. However, CXCL9 had no significant effect on the invasive spread capability in the CXCR3-KO group (Fig. 6D).

To accurately evaluate the cytotoxic effect of CD8$^+$ T cells within multicellular structures, we stained live cells with calcein AM and dead cells with EthD-1. Microscopic observations revealed that in the CXCR3-WT group, treating CD8$^+$ T cells with CXCL9 resulted in a substantial cell death rate among tumor cells. Knocking out CXCR3 reversed the cell death rate, leading to a partial recovery. There was no significant difference in cell death rate between the two groups within the CXCR3-WT group, further confirming the crucial role of the CXCL9-CXCR3 axis in regulating the cytotoxic function of CD8$^+$ T cells (Fig. 6E).

In conclusion, these experimental results demonstrate the critical regulatory role of the CXCL9-CXCR3 axis in CD8$^+$ T cells, significantly impacting the growth, invasion, and survival of tumor cells through their interaction.

In vivo experiments further indicate the promotion of CD8$^+$ T cell infiltration into tumor cells through the CXCL9-CXCR3 axis

Previous in vitro cell experiments have demonstrated the crucial role of CXCL9 in regulating the activity and cytotoxicity of CD8$^+$ T cells, a mechanism that may involve its impact on tumor cell proliferation and invasion. Subsequently, we intratumorally injected E0771 cells into the mammary fat pads of female C57BL/6 mice to establish an orthotopic tumor model (Fig. 7A). CD8$^+$ T cells from the CXCR3-WT and CXCR3-KO groups were then injected intratumorally or intravenously into the tumor-bearing mice. Injection was performed using 1×10^6 CFSE-labeled CD8$^+$ T cells, with near-infrared imaging conducted at 6h and 24h post-injection to track the distribution and infiltration of CD8$^+$ T cells in vivo (Fig. 7B). For imaging, specific wavelengths of lasers and corresponding filters were employed to detect the labeled CFSE signal. Mice that did not receive CD8$^+$ T cell injections served as the negative control group.

(See figure on next page.)

Fig. 6 Impact of CXCL9 on the cytotoxicity of CD8$^+$ T cells on tumor cells. *Note* **A** Cell Counting kit-8 (CCK-8) assessment of tumor cell proliferation at various time points; **B** Flow cytometry analysis of tumor cell apoptosis, with apoptotic cells marked in red boxes, and the right panel showing the statistical analysis of apoptotic cells; **C** Confocal microscopy images depicting the infiltration of CFSE-labeled CD8$^+$ T cells in the TME, with a scale bar of 25 μm, and the right panel presenting the statistical analysis of the average CFSE fluorescence intensity (FL) in TME; **D** Bright-field mode images of cell culture captured using an inverted microscope, outlining the invasive zone with a white dashed line, scale bar = 50 μm, and the right panel displaying the statistical analysis of the invasive area; **E** Confocal microscopy images of live/dead cell viability assay in the TME, with live cells stained with calcein-AM (green) and dead cells stained with EthD-1 (red), scale bar = 25 μm, and the right panel showing the statistical analysis of live/dead cells in TME. All cellular experiments were repeated thrice, with values presented as mean ± standard deviation, **indicating $P < 0.01$, and ***indicating $P < 0.001$

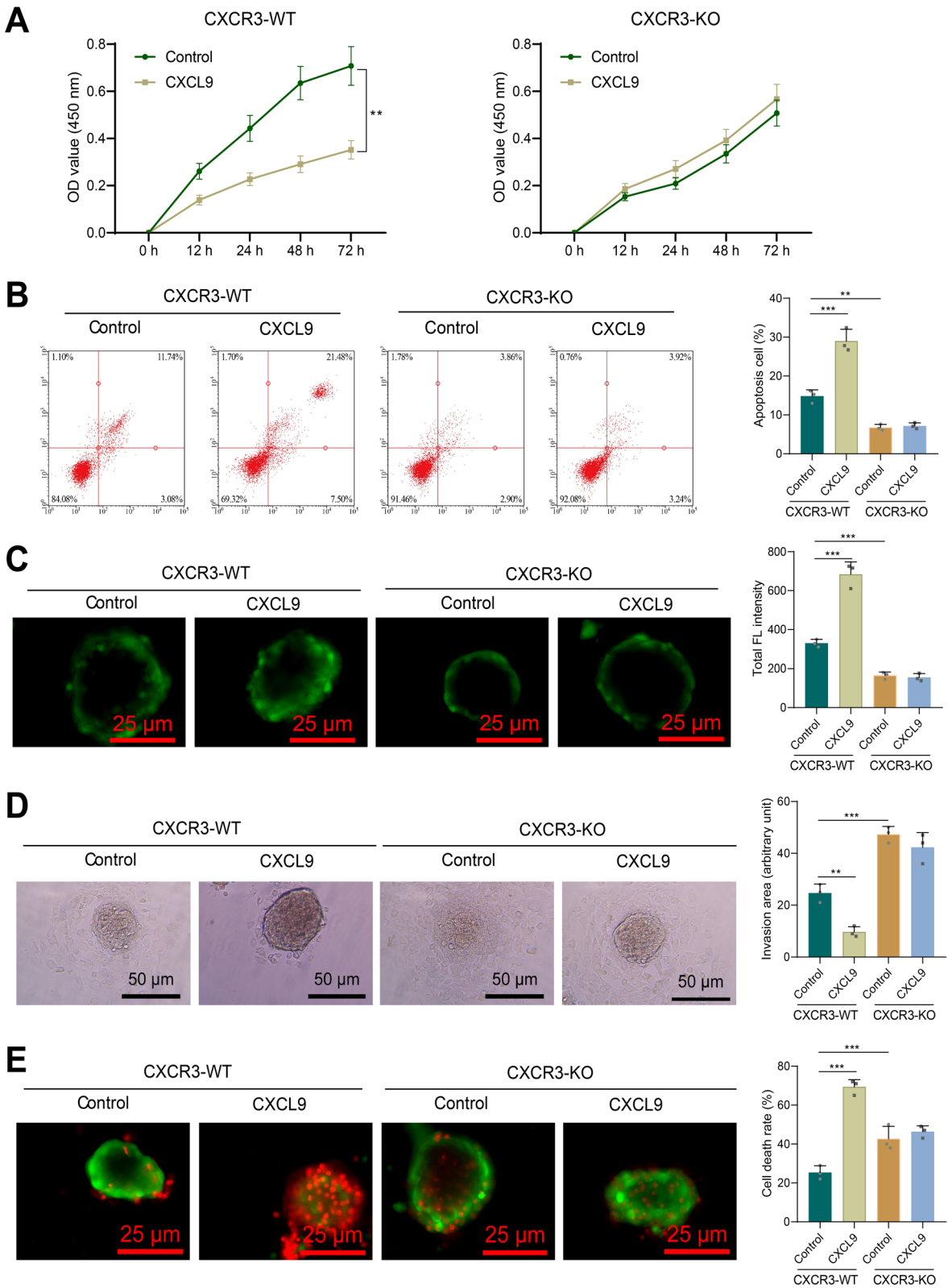

Fig. 6 (See legend on previous page.)

Imaging results revealed a significant increase in the accumulation of $CD8^+$ T cells in the CXCL9-treated group of CXCR3-WT mice compared to the untreated control group. Conversely, in CXCR3-KO mice, after CXCR3 deletion, there was a significant reduction in $CD8^+$ T cell accumulation, and this accumulation showed no significant difference with or without CXCL9 treatment (Fig. 7D). Subsequently, we performed ex vivo measurements by excising the tumors 24h after tail vein injection of different $CD8^+$ T cell groups to observe the infiltration capability of $CD8^+$ T cells in the tumor model. The results indicated that the CXCL9 group in the CXCR3-WT category had the highest accumulation of $CD8^+$ T cells compared to the Control group. Depletion of CXCR3 led to a significant decrease in $CD8^+$ T cell accumulation, while within the CXCR3-KO group, there was no significant difference in $CD8^+$ T cell accumulation between the two groups (Fig. 7E). To further assess the infiltration of $CD8^+$ T cells, we conducted immunofluorescence analysis. The results showed that CXCL9 treatment in the CXCR3-WT group resulted in widespread distribution of $CD8^+$ T cells away from tumor blood vessels, whereas CXCR3 knockout caused $CD8^+$ T cells to be confined around the vessels. Furthermore, there was no significant difference in $CD8^+$ T cell distribution between the two groups in the CXCR3-KO category (Fig. 7F). These findings indicate that CXCL9 enhances the infiltration capability of $CD8^+$ T cells into tumor tissues.

The above in vivo animal experiments further confirm the significant impact of altered expression of the CXCL9-CXCR3 axis on $CD8^+$ T cell infiltration in BRCA.

CXCR3 knockout reverses the antitumor immunity of FOLR2+ macrophages

To investigate whether FOLR2+ macrophages impact BRCA progression through CXCR3-mediated $CD8^+$ T cell activation, CXCR3 gene knockout ($CXCR3^{-/-}$) mice were generated, with normal (WT) mice as controls. Subsequently, an orthotopic tumor model was established, where FOLR2+ or FOLR2− macrophages were injected into the tumors, and tumor growth in mice was observed (Fig. 7C). $CD8^+$ T cell activation was assessed using flow cytometry and ELISA. The efficiency of CXCR3 knockout is shown in Fig. S10. Results revealed that in WT mice, compared to the FOLR2− macrophage group, mice in the FOLR2+ macrophage group exhibited slower tumor growth, smaller tumor size, and a lower proportion of ki67-positive cells. CXCR3 knockout promoted tumor growth in mice, leading to a higher proportion of ki67-positive cells. However, in $CXCR3^{-/-}$ mice, there was no significant difference in tumor volume or ki67-positive cell proportion between the two groups (Fig. 8A, B). These findings suggest that knocking out CXCR3 significantly reverses the tumor suppression effect of FOLR2+ macrophages.

Flow cytometry analysis of $CD8^+$ T cells within the tumors and spleens of mice from each group was conducted to determine the percentage of IFN-γ-positive cells, while ELISA was used to measure IFN-γ concentration in mouse serum. In WT mice, the group injected with FOLR2+ macrophages exhibited a higher proportion of IFN-γ-positive cells in both tumors and spleens, along with increased serum IFN-γ concentration compared to the FOLR2− macrophage group. Subsequent CXCR3 knockout resulted in decreased IFN-γ-positive cells in both tumors and spleens, accompanied by reduced serum IFN-γ levels. Notably, in $CXCR3^{-/-}$ mice, there was no significant difference in the percentage of IFN-γ-positive cells or serum IFN-γ concentration between the FOLR2− and FOLR2+ macrophage groups (Fig. 8C–E). These findings support the notion that knocking out CXCR3 significantly reverses the antitumor immune function of FOLR2+ macrophages.

Discussion

In recent years, macrophages have garnered significant attention in BRCA research, particularly regarding the potential role of FOLR2+ macrophages in regulating the TME [69–72]. This study utilized scRNA-seq and bulk RNA-seq techniques to reveal that FOLR2+ macrophages in BRCA tissue exhibit markedly enhanced interactions with $CD8^+$ T cells, aligning with previous research findings [56, 69–72]. These findings further

(See figure on next page.)

Fig. 7 Impact of the CXCL9-CXCR3 axis on the infiltration of $CD8^+$ T cells. *Note* **A**–**C** Schematic diagrams illustrating the in vivo model construction for each group; **D** Within 6 h after intratumoral injection of 1×10^6 CFSE-labeled $CD8^+$ T cells into the mammary gland, in vivo imaging was performed using a specific wavelength of near-infrared laser to observe the distribution of $CD8^+$ T cells in the tumor. The image on the right semi-quantitatively displays the $CD8^+$ T cell signal within the tumor, with mice not receiving $CD8^+$ T cells serving as the negative control; **E** Twenty-four hours after intravenous injection of labeled $CD8^+$ T cells via the tail vein, tumors were excised and imaged ex vivo using the same wavelength of near-infrared laser. The image on the right semi-quantitatively displays the $CD8^+$ T cell signal within the tumor; **F** Twenty-four hours after intravenous injection of labeled $CD8^+$ T cells via the tail vein, tumor sections were subjected to immunofluorescence analysis, with CFSE (green) labeling $CD8^+$ T cells, Cy3-labeled anti-CD31 antibody (red) staining tumor vasculature, and blue indicating cell nuclei. Scale bars = 100 μm. Each group consisted of 10 mice; numerical values represent mean ± standard deviation, and ***denotes significance at $P < 0.001$

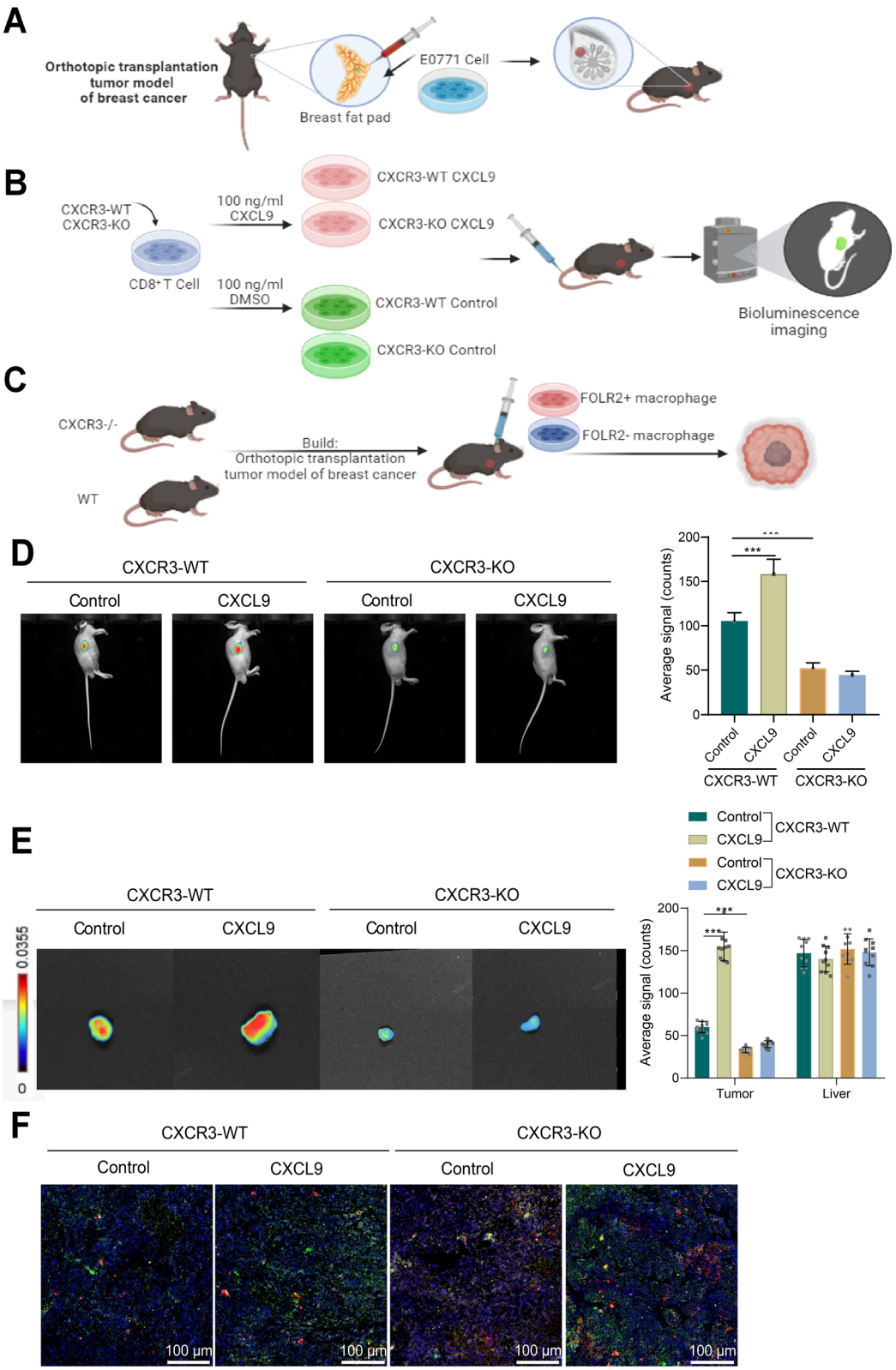

Fig. 7 (See legend on previous page.)

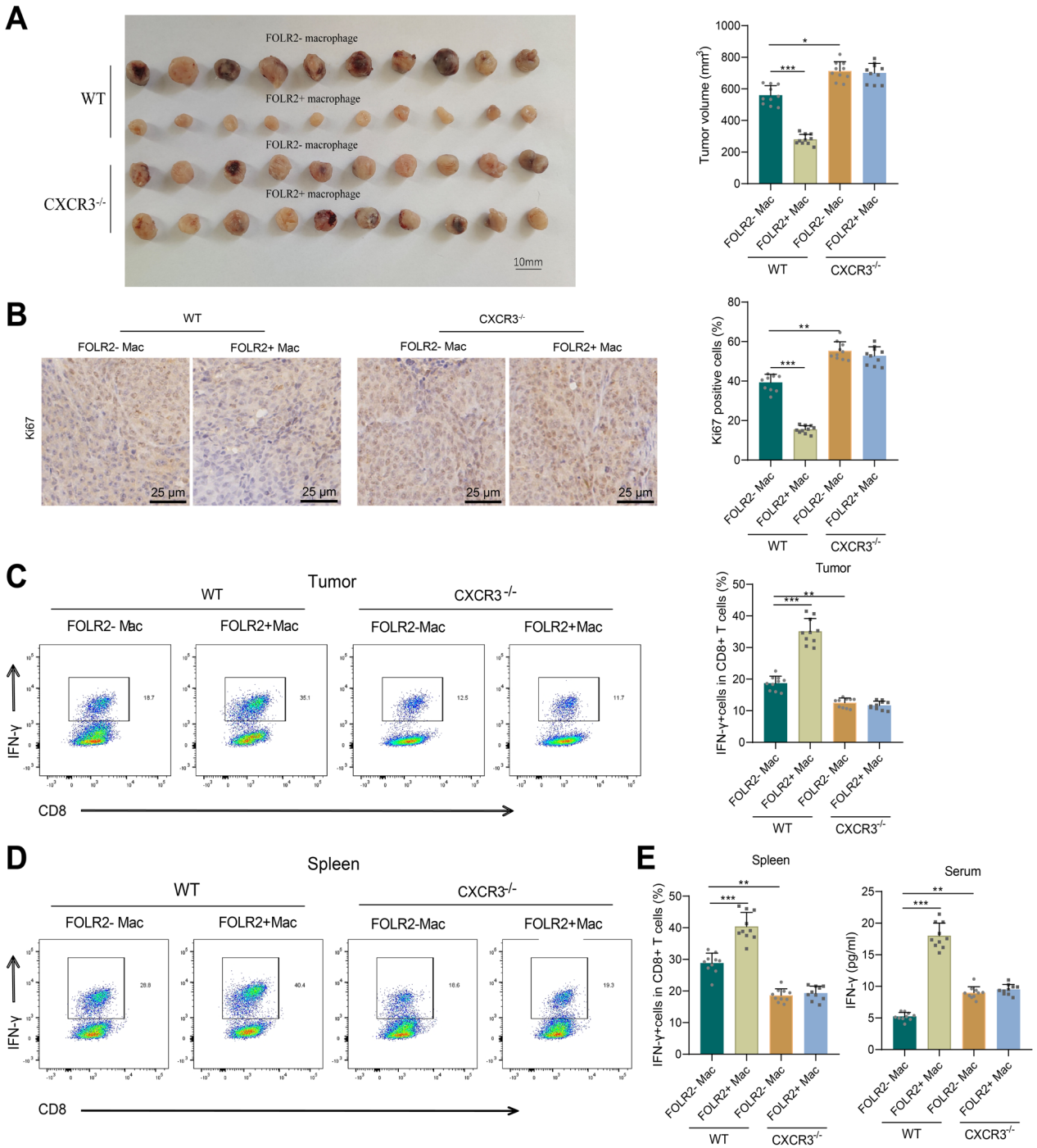

Fig. 8 The influence of CXCR3 deletion on the antitumor immunity of FOLR2+ macrophages. *Note* **A** Morphological images of tumor tissues from each group of mice and statistical analysis of tumor tissue volumes; **B** Immunohistochemical staining images (Ki67) of tumor tissues from each group of mice (scale bar: 25 μm) and statistical analysis of the proportion of positive cells; **C** Flow cytometry analysis showing the percentage of IFN-γ-positive cells in $CD8^+$ T cells in tumors of each group of mice, along with bar graphs for statistical comparison; **D** Flow cytometry analysis showing the percentage of IFN-γ-positive cells in $CD8^+$ T cells in the spleens of each group of mice, along with bar graphs for statistical comparison; **E** ELISA measurement of serum IFN-γ concentrations in each group of mice; *indicates $P < 0.05$, **indicates $P < 0.01$, ***indicates $P < 0.001$; there were 10 animals in each experimental group

substantiate the pivotal role of FOLR2+ macrophages in modulating the TME.

The TME of BRCA harbors a plethora of immune cells whose interactions and functional states directly impact tumor progression and treatment responses [73–75]. This study demonstrates significant alterations in cellular interactions within BRCA tissue compared to normal breast tissue, predominantly evident in paracrine/autocrine signaling pathways, aligning with previous research and underscoring the crucial role of the TME in BRCA initiation and progression [76]. Prior studies have confirmed the involvement of the CXCL9-CXCR3 axis in T cell infiltration and activation across various cancers [77]. This study unveils, for the first time in BRCA, that FOLR2+ macrophages primarily activate $CD8^+$ T cells via secretion of CXCL9 to bind with CXCR3, exerting anti-tumor effects and offering new targets for future therapeutic strategies.

BRCA is a highly heterogeneous disease, with distinct subtypes (e.g., ER+, HER2+, and TNBC) exhibiting significant differences in the immune microenvironment. Studies have shown that TNBC typically has higher levels of immune cell infiltration (e.g., CD8+ T cells and macrophages), and immune-related pathways such as the CXCL9-CXCR3 axis are likely more active in this subtype [78, 79]. In contrast, ER+ and HER2+ subtypes exhibit relatively weaker immune activity, which may influence the intensity of the CXCL9-CXCR3 axis. By constructing a CXCR3 gene knockout mouse model, this study further validated the antitumor immune role of FOLR2+ macrophages. Compared to previous studies, we have gained deeper insights into the relationship between FOLR2+ macrophages and the CXCL9-CXCR3 axis in BRCA. Additionally, the murine BRCA cell line E0771 was selected due to its high relevance to the TNBC subtype, particularly its extensive application in immune microenvironment studies. Although it is biased towards the TNBC subtype, its immune microenvironment characteristics provide a valuable reference for studying BRCA immunity. Future studies should incorporate subtype-specific data to verify whether the CXCL9-CXCR3 axis has universal regulatory functions across subtypes or is predominantly active in immunologically active BRCAs such as TNBC.

This study found that FOLR2 is associated with T cell immune infiltration in the TME of BRCA patients, consistent with prior findings indicating the beneficial impact of immune cell infiltration on tumor prognosis [80, 81]. Patients with high CXCL9 and CXCR3 expression exhibit better prognosis, providing clues for exploring the potential therapeutic value of this pathway in other cancers. By integrating scRNA-seq and bulk RNA sequencing (bulk RNA-seq), this study comprehensively analyzed the function of FOLR2+ macrophages at both macro and micro levels. This combined approach offers a deeper understanding of cell interactions compared to prior studies relying solely on a single technique, resulting in greater precision and explanatory power. Kumar et al. focused on macrophage subpopulations specific to normal breast tissue, such as macro-lipo and macro-IFN [26]. Complementing this, our study emphasizes the role of FOLR2+ macrophages in the tumor immune microenvironment of BRCA. In terms of data sources, this study not only relied on single-cell transcriptomic sequencing data (scRNA-seq), but also validated the findings using multiple independent public datasets, including the TCGA-BRCA dataset (overall transcriptomic data), the METABRIC dataset (overall transcriptomic data), the CPTAC dataset (proteomics data), the GEO database (transcriptomic data), and qPCR, Western blot, and immunofluorescence experiments from our own experimental cohort. These consistent data sources collectively support the important role of FOLR2+ macrophages in the breast cancer immune microenvironment and validate the expression changes of FOLR2 and its related signaling pathways in breast cancer patients. Therefore, this study did not incorporate additional scRNA-seq datasets for validation. Furthermore, single-cell sequencing results are often influenced by factors such as sample size, sequencing depth, and data noise. Direct subtype classification may lead to small sample sizes, which could affect the robustness of statistical analyses. Additionally, breast cancer exhibits significant internal heterogeneity, with multiple subtypes of cell populations possibly existing within a single tumor. For example, triple-negative breast cancer (TNBC) may contain some HER2-positive or ER+ cells, and HER2+ tumors may also contain ER+ cell populations. Classifying tumors into discrete subtypes may obscure the transcriptomic diversity within them. Therefore, the focus of this study was on exploring the single-cell atlas of breast cancer without delving into subtype-specific discussions of single-cell differences.

Based on these findings, we preliminarily conclude that FOLR2+ macrophages activate CD8+ T cells through the CXCL9-CXCR3 pathway, thereby exerting antitumor immune effects in BRCA (Fig. 9). This study successfully identified a macrophage subpopulation in BRCA, namely FOLR2+ macrophages, and explored their specific communication pathways in immune cells through clinical, cellular, and animal experiments. These findings may provide new theoretical insights into the specific mechanisms by which FOLR2+ macrophages exert antitumor immune effects. To better evaluate the clinical application potential of FOLR2+ macrophages in BRCA patients, larger-scale clinical studies and more comprehensive in vivo and in vitro experiments are needed.

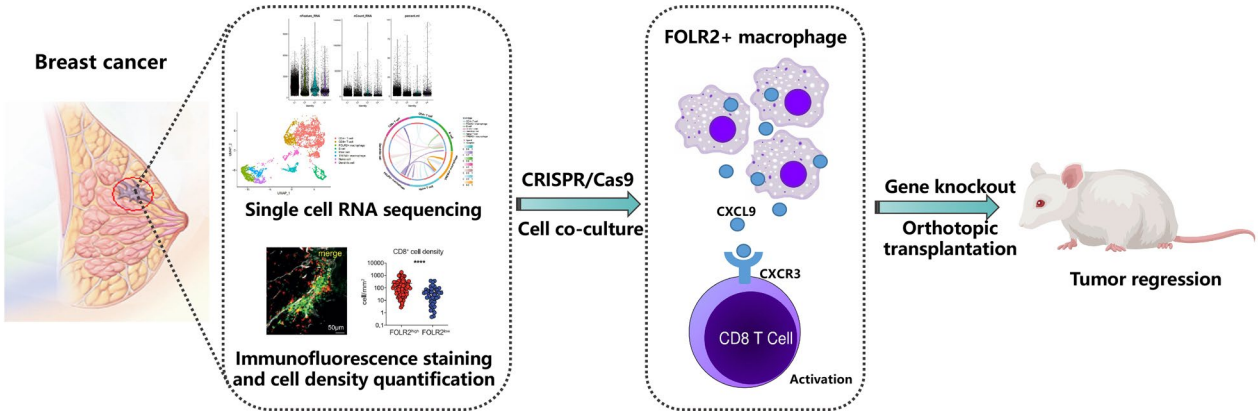

Fig. 9 Schematic representation of the molecular mechanism by which FOLR2+ macrophages activate $CD8^+$ T cells through the CXCL9-CXCR3 pathway to exert antitumor immunity in BRCA

Through scRNA-seq, this study has provided a detailed understanding of the cell types and their interactions in the TME of BRCA. The interaction between FOLR2+ macrophages and $CD8^+$ T cells has a particularly significant impact on the BRCA immune microenvironment. FOLR2+ macrophages were shown to activate $CD8^+$ T cells through the CXCL9-CXCR3 axis, thereby exerting anti-BRCA effects. This finding aligns with previous studies demonstrating that macrophages regulate T cell function via the CXCL family of chemokines [56, 82]. Additionally, research by Bassez et al. suggested that macrophage PD-L1 expression may further influence T cell function through immune checkpoint inhibition pathways [83]. Although this study did not directly examine PD-L1 expression in FOLR2+ macrophages, it provides a new direction for future research to explore the role of FOLR2+ macrophages in immune evasion mechanisms in BRCA.

Despite revealing the potential roles of FOLR2+ macrophages and their CXCL9-CXCR3 axis in BRCA, this study has several limitations. First, it has not been determined whether FOLR2+ macrophages influence tumor immune evasion through PD-L1 expression, which requires further experimental validation. Second, the distribution and function of FOLR2+ macrophages may vary significantly among different BRCA subtypes. Future research should involve larger sample sizes and subtype-specific analyses to confirm these findings. Additionally, the role of FOLR2+ macrophages and the CXCL9-CXCR3 axis in BRCA immunotherapy, such as anti-PD-1/PD-L1 therapy, warrants in-depth exploration. Such studies could aid in the development of novel immunotherapeutic strategies for BRCA patients.

In summary, this study provides new directions for BRCA immunotherapy but requires further research to validate and deepen these findings.

Supplementary Information

The online version contains supplementary material available at https://doi.org/10.1186/s13058-025-01980-4.

Additional file 1.
Additional file 2.
Additional file 3.
Additional file 4.
Additional file 5.
Additional file 6.
Additional file 7.
Additional file 8.
Additional file 9.
Additional file 10.
Additional file 11.
Additional file 12.

Acknowledgements
None.

Author contributions
Sixuan Wu, Baohong Jiang, and Zhimin Li contributed equally to this work and are considered co-first authors. Sixuan Wu and Zhimin Li conducted the in vivo and in vitro experiments and performed the data analysis. Baohong Jiang was responsible for bulk RNA sequencing and bioinformatics analysis. Yuanbin Tang, Lunqi Luo, Wenjie Feng, and Yiling Jiang provided critical experimental assistance and technical support. Yeru Tan and Yuehua Li supervised the study design, data interpretation, and manuscript preparation. All authors reviewed and approved the final manuscript.

Funding
This research was funded by the National Natural Science Foundation of China (No.82404928), Natural Science Foundation of Hunan Province (No. 2024JJ8232, 2023JJ60495, 2023JJ60496), Clinical Medical Research 4310 Program of the University of South China (No. 20224310NHYCG07) and Scientific Research Fund Project of Hunan Provincial Health Commission (No. B202303109577, D202303109450).

Data availability
All data can be provided as needed.

Declarations

Ethics approval and consent to participate

This study was approved by the Ethics Committee of the First Affiliated Hospital, Hengyang Medical School, University of South China and the methods were carried out in accordance with the approved guidelines. All the patients have been informed and signed informed consent before the experiments. The animal experimental processes were approved by the Ethnic Committee of the First Affiliated Hospital, Hengyang Medical School, University of South China and conducted in strict accordance to the standard of the Guide for the Care and Use of Laboratory Animals published by the Ministry of Science and Technology of the People's Republic of China in 2006.

Competing interests

The authors declare no competing interests.

Received: 9 September 2024 Accepted: 10 February 2025
Published online: 05 March 2025

References

1. Lei S, Zheng R, Zhang S, Wang S, Chen R, Sun K, et al. Global patterns of breast cancer incidence and mortality: a population-based cancer registry data analysis from 2000 to 2020. Cancer Commun. 2021;41:1183–94. https://doi.org/10.1002/cac2.12207.
2. Kashyap D, Pal D, Sharma R, Garg VK, Goel N, Koundal D, et al. [Retracted] Global increase in breast cancer incidence: risk factors and preventive measures. BioMed Res Int. 2022. https://doi.org/10.1155/2022/9605439.
3. Rojas K, Stuckey A. Breast cancer epidemiology and risk factors. Clin Obstet Gynecol. 2016;59:651–72. https://doi.org/10.1097/grf.0000000000000239.
4. Miao Q, Wang F, Dou J, Iqbal R, Muftuoglu M, Basar R, et al. Ab initio spillover compensation in mass cytometry data. Cytometry Pt A. 2020;99:899–909. https://doi.org/10.1002/cyto.a.24298.
5. So JY, Ohm J, Lipkowitz S, Yang L. Triple negative breast cancer (TNBC): non-genetic tumor heterogeneity and immune microenvironment: emerging treatment options. Pharmacol Ther. 2022;237: 108253. https://doi.org/10.1016/j.pharmthera.2022.108253.
6. Kawaguchi K, Maeshima Y, Toi M. Tumor immune microenvironment and systemic response in breast cancer. Med Oncol. 2022;39:208. https://doi.org/10.1007/s12032-022-01782-0.
7. Zheng G, Jia L, Yang A-G. Roles of HLA-G/KIR2DL4 in breast cancer immune microenvironment. Front Immunol. 2022;13: 791975. https://doi.org/10.3389/fimmu.2022.791975.
8. Lin J, Huang D, Xu H, Zhan F, Tan X. Macrophages: a communication network linking *Porphyromonas gingivalis* infection and associated systemic diseases. Front Immunol. 2022;13: 952040. https://doi.org/10.3389/fimmu.2022.952040.
9. Pan Y, Yu Y, Wang X, Zhang T. Tumor-associated macrophages in tumor immunity. Front Immunol. 2020;11: 583084. https://doi.org/10.3389/fimmu.2020.583084.
10. Cheng K, Cai N, Zhu J, Yang X, Liang H, Zhang W. Tumor-associated macrophages in liver cancer: from mechanisms to therapy. Cancer Commun. 2022;42:1112–40. https://doi.org/10.1002/cac2.12345.
11. Xiang X, Wang J, Lu D, Xu X. Targeting tumor-associated macrophages to synergize tumor immunotherapy. Sig Transduct Target Ther. 2021;6:75. https://doi.org/10.1038/s41392-021-00484-9.
12. Fan N, Zhang X, Zhao W, Zhao J, Luo D, Sun Y, et al. Covalent inhibition of pyruvate kinase M2 reprograms metabolic and inflammatory pathways in hepatic macrophages against non-alcoholic fatty liver disease. Int J Biol Sci. 2022;18:5260–75. https://doi.org/10.7150/ijbs.73890.
13. Sharma A, Seow JJW, Dutertre C-A, Pai R, Blériot C, Mishra A, et al. Onco-fetal reprogramming of endothelial cells drives immunosuppressive macrophages in hepatocellular carcinoma. Cell. 2020;183:377-394.e21. https://doi.org/10.1016/j.cell.2020.08.040.
14. Moharil P, Wan Z, Pardeshi A, Li J, Huang H, Luo Z, et al. Engineering a folic acid-decorated ultrasmall gemcitabine nanocarrier for breast cancer therapy: dual targeting of tumor cells and tumor-associated macrophages. Acta Pharm Sin B. 2022;12:1148–62. https://doi.org/10.1016/j.apsb.2021.09.024.
15. Zhu J, Shen Y, Wang L, Qiao J, Zhao Y, Wang Q. A novel 12-gene prognostic signature in breast cancer based on the tumor microenvironment. Ann Transl Med. 2022;10:143–143. https://doi.org/10.21037/atm-21-6748.
16. Bugatti M, Bergamini M, Missale F, Monti M, Ardighieri L, Pezzali I, et al. A population of TIM4+FOLR2+ macrophages localized in tertiary lymphoid structures correlates to an active immune infiltrate across several cancer types. Cancer Immunol Res. 2022;10:1340–53. https://doi.org/10.1158/2326-6066.cir-22-0271.
17. Liu X, Xu X, Wu Z, Shan Q, Wang Z, Wu Z, et al. Integrated single-cell RNA-seq analysis identifies immune heterogeneity associated with KRAS/TP53 mutation status and tumor-sideness in colorectal cancers. Front Immunol. 2022. https://doi.org/10.3389/fimmu.2022.961350.
18. Dai S, Zeng H, Liu Z, Jin K, Jiang W, Wang Z, et al. Intratumoral CXCL13+CD8+T cell infiltration determines poor clinical outcomes and immunoevasive contexture in patients with clear cell renal cell carcinoma. J Immunother Cancer. 2021;9: e001823. https://doi.org/10.1136/jitc-2020-001823.
19. Farhood B, Najafi M, Mortezaee K. CD8+ cytotoxic T lymphocytes in cancer immunotherapy: a review. J Cell Physiol. 2018;234:8509–21. https://doi.org/10.1002/jcp.27782.
20. Raskov H, Orhan A, Christensen JP, Gögenur I. Cytotoxic CD8+ T cells in cancer and cancer immunotherapy. Br J Cancer. 2020;124:359–67. https://doi.org/10.1038/s41416-020-01048-4.
21. Sebastian A, Hum NR, McCool JL, Wilson SP, Murugesh DK, Martin KA, et al. Single-cell RNA-Seq reveals changes in immune landscape in post-traumatic osteoarthritis. Front Immunol. 2022. https://doi.org/10.3389/fimmu.2022.938075.
22. Luo G, Gao Q, Zhang S, Yan B. Probing infectious disease by single-cell RNA sequencing: progresses and perspectives. Comput Struct Biotechnol J. 2020;18:2962–71. https://doi.org/10.1016/j.csbj.2020.10.016.
23. Zheng H, Liu H, Ge Y, Wang X. Integrated single-cell and bulk RNA sequencing analysis identifies a cancer associated fibroblast-related signature for predicting prognosis and therapeutic responses in colorectal cancer. Cancer Cell Int. 2021. https://doi.org/10.1186/s12935-021-02252-9.
24. Hatogai K, Sweis RF. The tumor microenvironment of bladder cancer. In: Birbrair A, editor. Advances in experimental medicine and biology. Cham: Springer; 2020. p. 275–90. https://doi.org/10.1007/978-3-030-59038-3_17.
25. Xu M, Li Y, Li W, Zhao Q, Zhang Q, Le K, et al. Immune and stroma related genes in breast cancer: a comprehensive analysis of tumor microenvironment based on the cancer genome atlas (TCGA) database. Front Med. 2020. https://doi.org/10.3389/fmed.2020.00064.
26. Kumar T, Nee K, Wei R, He S, Nguyen QH, Bai S, et al. A spatially resolved single-cell genomic atlas of the adult human breast. Nature. 2023;620:181–91. https://doi.org/10.1038/s41586-023-06252-9.
27. Keefe F, Monzón-Sandoval J, Rosser AE, Webber C, Li M. Single-cell transcriptomics reveals conserved regulatory networks in human and mouse interneuron development. IJMS. 2023;24:8122. https://doi.org/10.3390/ijms24098122.
28. Shao X, Liao J, Lu X, Xue R, Ai N, Fan X. scCATCH: automatic annotation on cell types of clusters from single-cell RNA sequencing data. iScience. 2020;23: 100882. https://doi.org/10.1016/j.isci.2020.100882.
29. Xin S, Liu X, Li Z, Sun X, Wang R, Zhang Z, et al. ScRNA-seq revealed an immunosuppression state and tumor microenvironment heterogeneity related to lymph node metastasis in prostate cancer. Exp Hematol Oncol. 2023. https://doi.org/10.1186/s40164-023-00407-0.
30. Chen K, Wang Y, Hou Y, Wang Q, Long D, Liu X, et al. Single cell RNA-seq reveals the CCL5/SDC1 receptor-ligand interaction between T cells and tumor cells in pancreatic cancer. Cancer Lett. 2022;545: 215834. https://doi.org/10.1016/j.canlet.2022.215834.
31. Zhang Y, Liu T, Hu X, Wang M, Wang J, Zou B, et al. Cell call: integrating paired ligand–receptor and transcription factor activities for cell–cell communication. Nucleic Acids Res. 2021;49:8520–34. https://doi.org/10.1093/nar/gkab638.
32. Efremova M, Vento-Tormo M, Teichmann SA, Vento-Tormo R. Cell PhoneDB: inferring cell–cell communication from combined expression

of multi-subunit ligand–receptor complexes. Nat Protoc. 2020;15:1484–506. https://doi.org/10.1038/s41596-020-0292-x.
33. Jin S, Guerrero-Juarez CF, Zhang L, Chang I, Ramos R, Kuan C-H, et al. Inference and analysis of cell–cell communication using cell chat. Nat Commun. 2021. https://doi.org/10.1038/s41467-021-21246-9.
34. Ritchie ME, Phipson B, Wu D, Hu Y, Law CW, Shi W, et al. limma powers differential expression analyses for RNA-sequencing and microarray studies. Nucleic Acids Res. 2015;43:e47–e47. https://doi.org/10.1093/nar/gkv007.
35. Yu G, Wang L-G, Han Y, He Q-Y. clusterProfiler: an R package for comparing biological themes among gene clusters. OMICS J Integr Biol. 2012;16:284–7. https://doi.org/10.1089/omi.2011.0118.
36. Wang L, Wang D, Yang L, Zeng X, Zhang Q, Liu G, et al. Cuproptosis related genes associated with Jab1 shapes tumor microenvironment and pharmacological profile in nasopharyngeal carcinoma. Front Immunol. 2022. https://doi.org/10.3389/fimmu.2022.989286.
37. Zhao W, Liu M, Zhang M, Wang Y, Zhang Y, Wang S, et al. Effects of inflammation on the immune microenvironment in gastric cancer. Front Oncol. 2021. https://doi.org/10.3389/fonc.2021.690298.
38. Song J, Yang R, Wei R, Du Y, He P, Liu X. Pan-cancer analysis reveals RIPK2 predicts prognosis and promotes immune therapy resistance via triggering cytotoxic T lymphocytes dysfunction. Mol Med. 2022. https://doi.org/10.1186/s10020-022-00475-8.
39. Newman AM, Liu CL, Green MR, Gentles AJ, Feng W, Xu Y, et al. Robust enumeration of cell subsets from tissue expression profiles. Nat Methods. 2015;12:453–7. https://doi.org/10.1038/nmeth.3337.
40. Du Y, Jiang X, Wang B, Cao J, Wang Y, Yu J, et al. The cancer-associated fibroblasts related gene CALD1 is a prognostic biomarker and correlated with immune infiltration in bladder cancer. Cancer Cell Int. 2021. https://doi.org/10.1186/s12935-021-01896-x.
41. Xu Y, Lin S, Tao J, Liu X, Zhou R, Chen S, et al. Correlation research of susceptibility single nucleotide polymorphisms and the severity of clinical symptoms in attention deficit hyperactivity disorder. Front Psychiatry. 2022. https://doi.org/10.3389/fpsyt.2022.1003542.
42. Sha S, Si L, Wu X, Chen Y, Xiong H, Xu Y, et al. Prognostic analysis of cuproptosis-related gene in triple-negative breast cancer. Front Immunol. 2022. https://doi.org/10.3389/fimmu.2022.922780.
43. Wang C, Ren Y-L, Zhai J, Zhou X-Y, Wu J. RETRACTED ARTICLE: Down-regulated LAMA4 inhibits oxidative stress-induced apoptosis of retinal ganglion cells through the MAPK signaling pathway in rats with glaucoma. Cell Cycle. 2019;18:932–48. https://doi.org/10.1080/15384101.2019.1593645.
44. Wu Q, Yi X. Down-regulation of long noncoding RNA MALAT1 protects hippocampal neurons against excessive autophagy and apoptosis via the PI3K/Akt signaling pathway in rats with epilepsy. J Mol Neurosci. 2018;65:234–45. https://doi.org/10.1007/s12031-018-1093-3.
45. Wang X, Wu Y. Protective effects of autophagy inhibitor 3-methyladenine on ischemia–reperfusion-induced retinal injury. Int Ophthalmol. 2020;40:1095–101. https://doi.org/10.1007/s10792-019-01272-9.
46. Lu X, Xuan W, Li J, Yao H, Huang C, Li J. AMPK protects against alcohol-induced liver injury through UQCRC2 to up-regulate mitophagy. Autophagy. 2021;17:3622–43. https://doi.org/10.1080/15548627.2021.1886829.
47. Li W, Zhang S, Liu J, Liu Y, Liang Q. Vitamin K2 stimulates Mc3T3-E1 osteoblast differentiation and mineralization through autophagy induction. Mol Med Rep. 2019. https://doi.org/10.3892/mmr.2019.10040.
48. Zhou S, Meng F, Du S, Qian H, Ding N, Sha H, et al. Bifunctional iRGD-anti-CD3 enhances antitumor potency of T cells by facilitating tumor infiltration and T-cell activation. J Immunother Cancer. 2021;9:e001925. https://doi.org/10.1136/jitc-2020-001925.
49. Lyu ZJ, Wang Y, Huang JL, Chen M, Wu SY, Yan Q, et al. Recurrent ZNF83-E293V mutation promotes bladder cancer progression through the NF-κB pathway via transcriptional dysregulation of S100A8. Mol Ther. 2021;29:275–90. https://doi.org/10.1016/j.ymthe.2020.09.004.
50. Wang W, Green M, Choi JE, Gijón M, Kennedy PD, Johnson JK, et al. CD8+ T cells regulate tumour ferroptosis during cancer immunotherapy. Nature. 2019;569:270–4. https://doi.org/10.1038/s41586-019-1170-y.
51. Zhu S, Zhu Z, Ma A-H, Sonpavde GP, Cheng F, Pan C. Preclinical models for bladder cancer research. Hematol Oncol Clin N Am. 2021;35:613–32. https://doi.org/10.1016/j.hoc.2021.02.007.
52. Zhang X, Zhao Y, Kong P, Han M, Li B. Expression of circZNF609 is down-regulated in colorectal cancer tissue and promotes apoptosis in colorectal cancer cells by upregulating. Med Sci Monit. 2019;25:5977–85.
53. Cheng C-C, Ho A-S, Peng C-L, Chang J, Sie Z-L, Wang C-L, et al. Sorafenib suppresses radioresistance and synergizes radiotherapy-mediated CD8+ T cell activation to eradicate hepatocellular carcinoma. Int Immunopharmacol. 2022;112: 109110. https://doi.org/10.1016/j.intimp.2022.109110.
54. Zeng X, Yao B, Liu J, Gong G-W, Liu M, Li J, et al. The SMARCA4R1157W mutation facilitates chromatin remodeling and confers PRMT1/SMARCA4 inhibitors sensitivity in colorectal cancer. NPJ Precis Oncol. 2023. https://doi.org/10.1038/s41698-023-00367-y.
55. Nishiyama T, Zhang Y, Cui M, Li H, Sanchez-Ortiz E, McAnally JR, et al. Precise genomic editing of pathogenic mutations in RBM20 rescues dilated cardiomyopathy. Sci Transl Med. 2022. https://doi.org/10.1126/scitranslmed.ade1633.
56. Nalio Ramos R, Missolo-Koussou Y, Gerber-Ferder Y, Bromley CP, Bugatti M, Núñez NG, et al. Tissue-resident FOLR2+ macrophages associate with CD8+ T cell infiltration in human breast cancer. Cell. 2022;185:1189-1207.e25. https://doi.org/10.1016/j.cell.2022.02.021.
57. He W, Zhang H, Han F, Chen X, Lin R, Wang W, et al. CD155T/TIGIT signaling regulates CD8+ T-cell metabolism and promotes tumor progression in human gastric cancer. Can Res. 2017;77:6375–88. https://doi.org/10.1158/0008-5472.can-17-0381.
58. Tong D, Zhao Y, Tang Y, Ma J, Wang Z, Li C. Circ-Usp10 promotes microglial activation and induces neuronal death by targeting miRNA-152-5p/CD84. Bioengineered. 2021;12:10812–22. https://doi.org/10.1080/21655979.2021.2004362.
59. Zhou K-X, Huang S, Hu L-P, Zhang X-L, Qin W-T, Zhang Y-L, et al. Increased nuclear transporter KPNA2 contributes to tumor immune evasion by enhancing PD-L1 expression in PDAC. J Immunol Res. 2021;2021:1–13. https://doi.org/10.1155/2021/6694392.
60. Shen J, Yang D, Zhou X, Wang Y, Tang S, Yin H, et al. Role of autophagy in zinc oxide nanoparticles-induced apoptosis of mouse LEYDIG cells. IJMS. 2019;20:4042. https://doi.org/10.3390/ijms20164042.
61. Lin Y-N, Schmidt MO, Sharif GM, Vietsch EE, Kiliti AJ, Barefoot ME, et al. Impaired CXCL12 signaling contributes to resistance of pancreatic cancer subpopulations to T cell-mediated cytotoxicity. OncoImmunology. 2022. https://doi.org/10.1080/2162402x.2022.2027136.
62. Zhang Y, Ning C, Zhou H, Yan Y, Liu F, Huang Y. Interleukin-1β, interleukin-6, and interleukin-17A as indicators reflecting clinical response to celecoxib in ankylosing spondylitis patients. Ir J Med Sci. 2020;190:631–8. https://doi.org/10.1007/s11845-020-02366-5.
63. Gomes-Santos IL, Amoozgar Z, Kumar AS, Ho WW, Roh K, Talele NP, et al. Exercise training improves tumor control by increasing CD8+ T-cell infiltration via CXCR3 signaling and sensitizes breast cancer to immune checkpoint blockade. Cancer Immunol Res. 2021;9:765–78. https://doi.org/10.1158/2326-6066.cir-20-0499.
64. Carpenter KJ, Valfort A-C, Steinauer N, Chatterjee A, Abuirqeba S, Majidi S, et al. LXR-inverse agonism stimulates immune-mediated tumor destruction by enhancing CD8 T-cell activity in triple negative breast cancer. Sci Rep. 2019. https://doi.org/10.1038/s41598-019-56038-1.
65. Stibbe JA, Hoogland P, Achterberg FB, Holman DR, Sojwal RS, Burggraaf J, et al. Highlighting the undetectable—Fluorescence molecular imaging in gastrointestinal endoscopy. Mol Imaging Biol. 2022;25:18–35. https://doi.org/10.1007/s11307-022-01741-1.
66. Zhang Q-F, Li J, Jiang K, Wang R, Ge J, Yang H, et al. CDK4/6 inhibition promotes immune infiltration in ovarian cancer and synergizes with PD-1 blockade in a B cell-dependent manner. Theranostics. 2020;10:10619–33. https://doi.org/10.7150/thno.44871.
67. Onkar SS, Carleton NM, Lucas PC, Bruno TC, Lee AV, Vignali DAA, et al. The great immune escape: Understanding the divergent immune response in breast cancer subtypes. Cancer Discov. 2022;13:23–40. https://doi.org/10.1158/2159-8290.cd-22-0475.
68. Wang Y, Klijn JG, Zhang Y, Sieuwerts AM, Look MP, Yang F, et al. Gene-expression profiles to predict distant metastasis of lymph-node-negative primary breast cancer. Lancet. 2005;365:671–9. https://doi.org/10.1016/s0140-6736(05)17947-1.

69. Müller A, Köhler UA, Trzebanski S, Vinik Y, Raj HM, Girault J, et al. Mouse modeling dissecting macrophage-breast cancer communication uncovered roles of PYK2 in macrophage recruitment and breast tumorigenesis. Adv Sci. 2022. https://doi.org/10.1002/advs.202105696.
70. Mehta AK, Kadel S, Townsend MG, Oliwa M, Guerriero JL. Macrophage biology and mechanisms of immune suppression in breast cancer. Front Immunol. 2021. https://doi.org/10.3389/fimmu.2021.643771.
71. Choi et al. Histol Histopathol, vol 33. Available from: http://www.hh.um.es/Abstracts/Vol_33/33_2/33_2_133.htm.
72. Qiu S-Q, Waaijer SJH, Zwager MC, de Vries EGE, van der Vegt B, Schröder CP. Tumor-associated macrophages in breast cancer: Innocent bystander or important player? Cancer Treat Rev. 2018;70:178–89. https://doi.org/10.1016/j.ctrv.2018.08.010.
73. Majidpoor J, Mortezaee K. The efficacy of PD-1/PD-L1 blockade in cold cancers and future perspectives. Clin Immunol. 2021;226: 108707. https://doi.org/10.1016/j.clim.2021.108707.
74. Mao X, Xu J, Wang W, Liang C, Hua J, Liu J, et al. Crosstalk between cancer-associated fibroblasts and immune cells in the tumor microenvironment: new findings and future perspectives. Mol Cancer. 2021. https://doi.org/10.1186/s12943-021-01428-1.
75. Lei X, Lei Y, Li J-K, Du W-X, Li R-G, Yang J, et al. Immune cells within the tumor microenvironment: biological functions and roles in cancer immunotherapy. Cancer Lett. 2020;470:126–33. https://doi.org/10.1016/j.canlet.2019.11.009.
76. Yang W-H, Cha J-H, Xia W, Lee H-H, Chan L-C, Wang Y-N, et al. Juxtacrine signaling inhibits antitumor immunity by upregulating PD-L1 expression. Can Res. 2018;78:3761–8. https://doi.org/10.1158/0008-5472.can-18-0040.
77. Jandl K, Marsh LM, Mutgan AC, Crnkovic S, Valzano F, Zabini D, et al. Impairment of the NKT–STAT1–CXCL9 axis contributes to vessel fibrosis in pulmonary hypertension caused by lung fibrosis. Am J Respir Crit Care Med. 2022;206:981–98. https://doi.org/10.1164/rccm.202201-0142oc.
78. Horikita F, Hashiguchi J, Nagashima T. Post colonoscopic Listeria monocytogenes meningitis in a patient with multiple myeloma during daratumumab-based therapy [J]. Rinsho Ketsueki. 2020;61(11):1611–1615. https://doi.org/10.11406/rinketsu.61.1611
79. Jike W, Sablok G, Bertorelle G, Li M, Varotto C. In silico identification and characterization of a diverse subset of conserved microRNAs in bioenergy crop *Arundo donax* L. Sci Rep. 2018. https://doi.org/10.1038/s41598-018-34982-8.
80. Tanaka A, Sakaguchi S. Regulatory T cells in cancer immunotherapy. Cell Res. 2016;27:109–18. https://doi.org/10.1038/cr.2016.151.
81. Bruni D, Angell HK, Galon J. The immune contexture and immunoscore in cancer prognosis and therapeutic efficacy. Nat Rev Cancer. 2020;20:662–80. https://doi.org/10.1038/s41568-020-0285-7.
82. Li Y, Huang K, Cheng Y, Tong Y, Mo J. Pain management by nurses in level 2 and level 3 hospitals in China. Pain Manag Nurs. 2019;20:284–91. https://doi.org/10.1016/j.pmn.2018.08.002.
83. Bassez A, Vos H, Van Dyck L, Floris G, Arijs I, Desmedt C, et al. A single-cell map of intratumoral changes during anti-PD1 treatment of patients with breast cancer. Nat Med. 2021;27:820–32. https://doi.org/10.1038/s41591-021-01323-8.

Publisher's Note